8-2019

Using Origami Folding Techniques to Study the Effect of Non-Linear Stiffness on the Performance of Jumping Mechanism

Blake Betsill
Clemson University, bbetsil@clemson.edu

USING ORIGAMI FOLDING TECHNIQUES TO STUDY THE EFFECT OF NON-LINEAR STIFFNESS ON THE PERFORMANCE OF JUMPING MECHANISMS

A Thesis
Presented to
the Graduate School of
Clemson University

In Partial Fulfillment
of the Requirements for the Degree
Master of Science
Mechanical Engineering

---

by
Blake Daniel Betsill
August 2019

Accepted by:
Dr. Suyi Li, Committee Chair
Dr. Phanindra Tallapragada
Dr. Todd Schweisinger

ABSTRACT

This research uses Origami patterns and folding techniques to generate non-linear force displacement profiles and study their effect on jumping mechanisms. In this case, the jumping mechanism is comprised of two masses connected by a Tachi-Miura Polyhedron (TMP) with non-linear stiffness characteristics under tensile and compressive loads. The strain-softening behavior exhibited by the TMP enables us to optimize the design of the structure for improved jumping performance. I derive the equations of motion of the jumping process for the given mechanism and combine them with the kinematics of the TMP structure to obtain numerical solutions for the optimum design. The results correlate to given geometric configurations for the TMP that result in the two optimum objectives: The maximum time spent in the air and maximum clearance off the ground. I then physically manufacture the design and conduct compression tests to measure the force-displacement response and confirm it with the theoretical approach based on the kinematics. Experimental data from the compression tests show a hysteresis problem where the force-displacement profile exhibits different behavior whether the structure is being compressed or released. I investigate two methods to nullify the hysteresis when compressing or releasing the mechanism and then discuss their results. This research can lead to easily manufacturable jumping robotic mechanisms with improved energy storage and jumping performance. Additionally, I learn more about how to use origami techniques to harness unique stiffness properties and apply them to a variety of scenarios.

DEDICATION

This thesis is dedicated to my family. The love and support I have received from all of you during my 7 years at Clemson has made this journey possible. Thank you and I love you all!

ACKNOWLEDGMENTS

I would first like to thank Dr. Suyi Li for his help and guidance throughout this project. Dr. Li provided the necessary equipment, funding, and background knowledge with Origami structures to make this project possible. Dr. Li also helped to keep the research focused and moving at a regular pace. His efforts were instrumental to the completion of this thesis.

I would also like to give special acknowledgement to Sahand Sadeghi for working as a partner for a large body of work that was necessary for the progress of this thesis. Sahand was the primary effort behind defining the dynamics of the jumping mechanism under study. His work investigating how non-linear stiffness profiles affect the performance of generic jumping mechanisms allowed for the adaptation to the TMP Origami structure.

Thirdly, I would like to thank Dr. Phanindra Tallapragada and Dr. Georges Fadel. Dr. Tallapragada provided the inspiration for studying dynamic jumping mechanisms that use elastic energy storage as their means of actuation, specifically those exhibiting non-linear force-displacement profiles. Dr. Fadel provided the inspiration to utilize optimization techniques on the TMP design to optimize the jumping performance.

Special thanks to Dr. Todd Schweisinger for serving on my committee as well as giving me the opportunity to serve as a TA throughout my duration of time working on this project. The assistantship provided the necessary personal funding to make this project possible. I additionally gained many new skills and learned a lot about leadership, teaching, and communication during my time as a TA.

Finally, I would like to thank Clemson University, the Mechanical Engineering Department, and my fellow graduate students for the support in all areas necessary to complete this thesis.

Additional Thanks:

Dr. Joshua Summers

Dr. Rachel Anderson

Dr. Nicole Coutris

Dr. Gang Li

Dr. Yue Wang

Dr. Richard S. Figliola

Trish Nigro

Gwen Dockins

Kathryn Poole

Melissa Kaisner

Beau Pollard

Ryan Geer

Nafiseh Masoudi

Devin Keck

Mitra Shabani

Saheem Absar

Zibusiso Dhlamini

Taylor Nichols

Nicholas Spivey

Jake Buzhardt

Jacob Biddlecom

Sindora Baddam

Tyler Ward

John Kremar

William McCormack

Nicole Zero

Caroline Buck

TABLE OF CONTENTS

TITLE PAGE i

ABSTRACT ii

DEDICATION iii

ACKNOWLEDGMENTS iv

Additional Thanks v

LIST OF TABLES ix

LIST OF FIGURES x

CHAPTER ONE:
INTRODUCTION AND REVIEW 1

1.1 Introduction 1

1.2 Review of the Dynamics of a Jumping Mechanism 4

1.2.1 Pre-Jump Phase 7

1.2.2 Post-Jump Phase 8

1.3 Review of the Effect of Non-Linear Force Displacement Profiles on Jumping Behavior. 9

1.3.1 Energy Storage in the Compressed Region of the Force Displacement Curve 10

1.3.2 Tensile Region of the Force-Displacement Curve and Its Effect on Internal Oscillation in the Post-Jump Phase 17

CHAPTER TWO:
USING THE TACHI-MIURA POLYHEDRON (TMP) BELLOWS TO ACHIEVE NON- LINEAR FORCE DISPLACEMENT BEHAVIOR 24

2.1 Defining the Geometry and Force Displacement Profile of the TMP Bellows 24

2.2 Optimizing the TMP Bellows Design for Improved Jumping Performance 29

Table of Contents (Continued) Page

CHAPTER THREE:
EXPERIMENTAL CONFIRMATION OF NON-LINEAR FORCE DISPLACEMENT PROFILE IN THE TMP BELLOWS 36

3.1 Manufacturing of the TMP and Crease-line Modifications and Their Effect on Torsional Fold Stiffness 36

3.2 Force Displacement Profile of Original Versus Optimized TMP Design 47

3.3 Hysteresis Behavior in the TMP Bellows Force Displacement Profile 52

3.3.1 Percent Energy Loss Due to Hysteresis in TMP Bellows 53

3.3.2 Introducing Torsional Springs to the TMP Bellows Sub-Folds 57

CHAPTER FOUR:
CONCLUSIONS AND RECOMMENDATIONS FOR FUTURE RESEARCH 62

APPENDICES 65

REFERENCES 70

LIST OF TABLES

Table 1: The design variables and geometric constraints used in the design optimization..... 31

Table 2: Other design variables used in the optimization..... 32

Table 3: Optimized TMP Bellows designs for Airtime and Clearance Objectives..... 33

Table 4: Original Design Stored Energy..... 52

Table 5: Optimized Design Stored Energy..... 52

Table 6: Optimized Design Energy Lost due to Hysterical Error..... 55

Table 7: Original Design Energy Lost due to Hysterical Error..... 56

Table 8: Stored and Lost Energy for TMP with Torsional Springs and Weakened Sub-Folds..... 60

Table 9: Stored and Lost Energy for TMP with Torsional Springs and Strengthened Sub-Folds.....61

LIST OF FIGURES

Figure 1: Schematic of the jumping mechanism..... 5

Figure 2: Piecewise linear reaction force-displacement curve of spring with structural and actuation limits..... 6

Figure 3: Reaction force-displacement curve 10

Figure 4: Three different piecewise linear force-displacement curves, with positive, negative and zero 3ˆk stiffness coefficients. 13

Figure 5: Gravitational potential energy levels of the upper mass (UM), lower mass (LM) and center of gravity (CG) 15

Figure 6: Three different piecewise linear force-displacement curves with the same compression section 18

Figure 7: Vertical displacement of the upper mass (solid line) and the lower mass (dashed line). 19

Figure 8: Design of the Tachi-Miura Polyhedron (TMP) bellow. 25

Figure 9: The force-displacement curve of a TMP bellow. 27

Figure 10: A typical time response of the TMP origami jumper. 30

Figure 11: Pareto front obtained in the optimization results..... 35

Figure 12: Solidworks Model of the Back Side Crease Lines for one of the 2 Sheets Necessary for the TMP Bellows 38

Figure 13: Adobe Illustrator file for the Back Side Crease Lines for one of the 2 Sheets Necessary for the TMP Bellows. 39

Figure 14: The FCX4000 Cutter In progress 40

Figure 15: The back side of one Sheet Necessary for the TMP before folding..... 41

Figure 16: TMP Bellows Manufactured from Paper 42

Figure 17: Original TMP Bellows Design Manufactured from Polypropylene 42

Figure 18: Optimized TMP Bellows Design Manufactured from Polypropylene..... 42

Figure 19: The Load Cell and Experiment Setup for the TMP Compression Tests..... 44

Figure 20: The Optimized TMP Undergoing a Compression Test..... 45

Figure 21: Optimized Design with Strengthened Sub Folds compared to Weakened Sub Folds..... 46

Figure 22: FD Curves for Original Design vs Optimized Design 48

Figure 23: Experimental FD Curves for OG vs Optimized Design..... 49

Figure 24: Theoretical vs Experimental FD Curve for Original Design showing Comparable Linear Stiffness..... 50

Figure 25: Theoretical vs Experimental FD Curve for Optimized Design showing Comparable Linear Stiffness..... 51

Figure 26: Compression vs Release Force Displacement Curve for Optimized Design .. 54

Figure 27: Compression vs Release Force Displacement Curve for Original Design..... 56

Figure 28: Optimized TMP with Torsional Springs 58

Figure 29: TMP Bellows with Weakened Crease Lines and Torsional Springs mounted along each Sub Fold..... 59

Figure 30: TMP Bellows with Strengthened Crease Lines and Torsional Springs mounted along each Sub Fold..... 60

CHAPTER ONE

INTRODUCTION AND REVIEW

1.1 Introduction

The invention of robots has greatly advanced human technologies in a variety of applications. From industrial [1]–[3] and military [4] applications to education [5], [6] and healthcare [7], [8] robots are improving the overall quality of our lives. Of particular note is the use of robots in different exploration scenarios. The use of robots allows for the exploration and investigation of different environments that would be too hazardous for humans to search on their own [9]. One of the challenges in developing robots for different exploratory tasks is deciding on the appropriate method of locomotion, be it wheeled, tracked, legged, or aviatory [10] . The advantage of using legged locomotion in mobile robots is that they are able to traverse uniquely challenging terrain that would otherwise be inaccessible to wheeled or tracked robots such as steep or sheer cliffs, rock shelves, or extremely soft terrain like deep sand or mud [11].

Legged robots however require complex non-linear control due to their more complicated motion dynamics and ground impacts [12]. To simplify this, researchers can use single legged robots that utilize jumping as their form of motion [13]–[16]. The most important part of jumping performance relates to the storage of energy and its rapid release [12], [13], [17], [18]. The stored energy of the system prior to the jump transitions to the kinetic energy of the mechanism during the jump, and the maximum gravitational potential energy at peak jump height. In this way, an increase in stored energy prior to jumping

directly translates to greater gravitational potential energy and therefore a higher jump. There are various methods for energy storage in jumping robots including traditional linear springs [19]–[21], compressed air [22], and custom elastic elements [23]–[25]. Traditional linear springs can be compressed and store potential energy directly related to Hooke's law. Suddenly releasing the springs will lead to a rapid release of the stored energy and force the system upwards into a jump. Compressed air can be used as the driving force on a cylinder that rapidly extends against the ground to launch the robot into the air. Higher pressures or greater volumes of air lead to greater stored energy of the system and greater jump height similarly to the traditional linear springs. Elastic elements work much the same way as the springs, being compressed or deformed to store some elastic strain energy. In the study by Yamada et al., the snap-through buckling of a closed elastic element is examined as a means of energy storage [25], [26]. In the case of jumping mechanisms, the restorative force of the elements is used as the actuation method to push the robot upwards into the air.

Non-linear spring elements with strain-softening behavior can be especially advantageous in the storage of strain energy versus their linear counter-parts. By storing more strain energy, the jumping performance can be improved in terms of reaching a greater center of gravity height as well as a higher clearance off the ground. Fiorini and Burdick investigated a jumping mechanism that achieves non-linear stiffness by implementing a linear spring in a 6-bar geared mechanism [27]. The improved jumping performance for non-linear spring elements versus linear elements does come at a small sacrifice of energy efficiency of the system. However, the loss in efficiency is small

compared to that of the improved jump height for the center of gravity of the system and its clearance from the ground [17]. Therefore, in most cases using non-linear spring elements can be advantageous to improve the jumping performance of a jumping mechanism where maximum energy efficiency is not critical. The challenge lies in achieving the appropriate non-linear stiffness behavior.

Origami, the ancient Japanese art of paper folding, has recently allowed for the expansion in possible designs and manufacturing capabilities of engineers. From deployable structures [28], self-folding robots [29], to surgical devices [30], and DNA machines [31] we are learning more about the characteristics of origami designs and their possible applications. One particular area of note is the use of Origami folding techniques to achieve tunable non-linear stiffness properties within mechanical structures [32]–[35]. This research focuses on a specific origami folding pattern, the Tachi-Miura Polyhedron (referred to as the TMP, and shown later in Figure 8) [36], [37] as a method for achieving the desirable non-linear stiffness properties to improve jumping performance.

This research is organized as follows: first I look into the general method of utilizing non-linear stiffness to improve jumping performance by storing larger amounts of energy. This is done by developing and examining the equations of motion and kinematic relationship for a jumping mechanism defined by two masses connected by a generic non-linear spring element. From there, I define the specific kinematics of the TMP design and show how it can be used as the non-linear spring element in our jumping mechanism. Then I move into the optimization techniques used on the design of the TMP structure to maximize jumping performance based on our theoretical model and analysis. Finally, I demonstrate the

practicality of using the TMP as a viable non-linear spring element by experimentally confirming the force-displacement curve of the TMP to its theoretical model.

1.2 Review of the Dynamics of a Jumping Mechanism

This section reviews the effects of utilizing nonlinear springs on the performance of a jumping mechanism. The mechanism is defined by two masses interconnected by a generic nonlinear spring represented by a piecewise linear function. Non-dimensional equations of motion are derived for the system and are analyzed both analytically and numerically to observe the jumping performance of the system. The nonlinear force-displacement curve is broken into two sections and the effects from changes to their properties are studied separately. These sections are the compression region, when the mechanism is subject to a negative (downward) displacement, and the tension region, as the mechanism is subject to a positive (upwards) displacement. It is observed that changes to the compression region of the force-displacement curve can lead to significant increases in overall stored energy and therefore improved jumping performance. Changes to the tension region do not affect the jumping performance of the system in terms of the height achieved by the center of gravity. However, the tension region does affect the internal oscillations of the system during the jump and can therefore affect the maximum clearance of the system off the ground. Results of this study provide valuable insight into the necessary nonlinear behavior and shape of the force-displacement curve to improve jumping performance. This information for a generic jumping mechanism can then be adapted to a specific design used to generate the proper nonlinear properties.

The work for this section as well as section 1.3 has already been published and discussed extensively in [17] and the figures for these sections come directly from that paper.

The jumping mechanism (Figure 1) investigated consists of two identical masses connected by an elastic element exhibiting non-linear stiffness characteristics. Energy storage in the system occurs through exerting an input force using an actuator on the top mass to deform the elastic element.

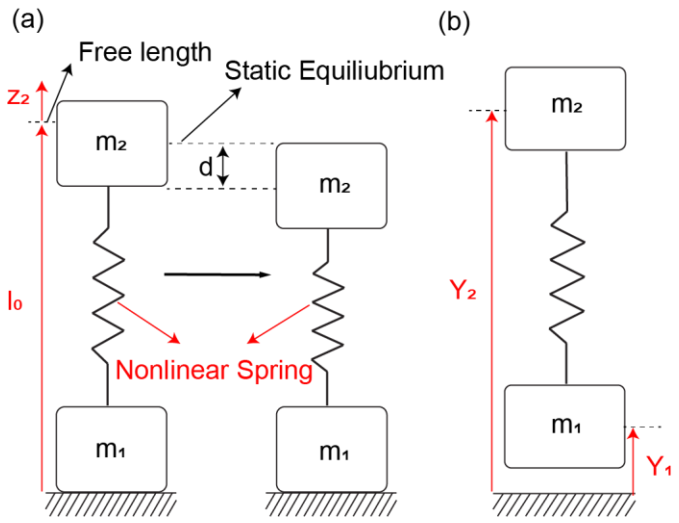

Figure 1: Schematic of the jumping mechanism in (a) pre-jump phase of motion and (b) post-jump phase of motion.

The reaction force-displacement relationship of the nonlinear spring can be generally represented by a C^n $(n \geq 0)$ continuous curve. However, in order to avoid introducing unnecessary complexities, I focus on a generic piecewise linear C^0 curve to describe the nonlinear stiffness properties. Despite its relative simplicity, the C^0 curve is a useful tool for approximating many nonlinear stiffness properties commonly used for engineering applications, e.g. negative stiffness [38] and quasi-zero stiffness [35], [39] characteristics.

Figure 2(a) shows the C^0 piecewise linear force-displacement curve that will be used in this study. The displacement axis is represented by y, where $y = Y_2 - Y_1 - l_0$. Y_1 and Y_2 are the height of the two masses with respect to the ground, and l_0 is the free length of the nonlinear spring. This curve consists of four linear sections with different stiffness coefficients (K_1 to K_4). We also consider the structural and actuation limit that can constrain the problem. The structural limit (H) is the maximum relative displacement between the two masses in order to compress the spring and store an initial energy.

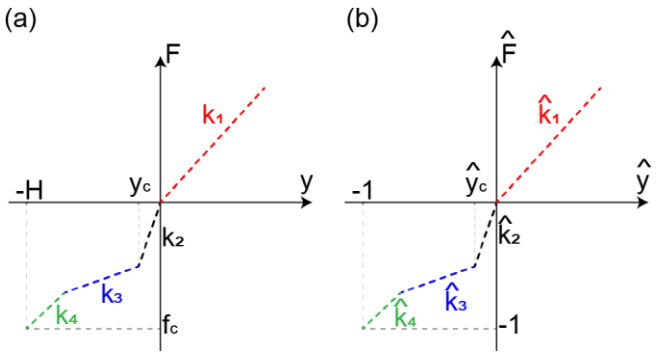

Figure 2: (a) Piecewise linear reaction force-displacement curve of spring with structural and actuation limits. (b) Non-dimensional force-displacement curve.

The actuation limit is the maximum amount of external force (f_c) the actuator can provide. Moreover, the force-displacement curve can be divided in to two separate regions: The compression region (negative displacement), where the spring is compressed; and the tension region (positive displacement), where the spring is under tension. This separation allows us to study the energy storage (compression) and jumping dynamics (tension) in a more systematic approach, as we will see later in sections 1.2.3 and 1.2.4.

Knowing the reaction force of the nonlinear spring, we can now investigate the dynamic behavior of the system. The dynamic motion of the jumping mechanism can be

divided into two different phases: 1) pre-jump phase and 2) post-jump phase. In order to just focus on the potential effects of the nonlinear spring, we assumed that the masses are equal: $m_1 = m_2 = m$. In the following two sections, we study the motion of the system in these two phases.

1.2.1 Pre-Jump Phase

The pre-jump phase (Figure 1(a)) occurs for all time prior to the bottom mass m_1 leaving the ground. During this phase, an input actuation force displaces m_2 down to a certain initial position (d). Once the input force is removed, the reaction force of the spring accelerates the upper mass upward. The governing equation of motion during this phase can be represented by:

$$m\ddot{Y}_2 = -F(Y_2 - l_0) - mg, \tag{1}$$

where m is the mass of the upper body, $F(Y_2 - l_0)$ is the reaction force of the spring, and $\ddot{Y}_2$ and Y_2 represent the acceleration and position of the upper mass (relative to the ground), respectively. We define $k^* = f_c / H$, the ratio between actuation limit and structural limit, as a reference linear spring coefficient. Equation (1) can be non-dimensionalized as follows:

$$\frac{d^2\hat{Y}_2}{d\tau^2} + \hat{F}(\hat{Y}_2 - \hat{l}_0) = -\hat{G}, \tag{2}$$

where, $\hat{Y}_1 = \frac{Y_1}{H}$, $\tau = t\omega$, $\omega = \sqrt{\frac{k^*}{m}}$, $\hat{F} = \frac{F}{f_c}$, $\hat{l}_0 = \frac{l_0}{H}$ and $\hat{G} = \frac{mg}{f_c}$. We can also non-dimensionalize the stiffness coefficients: $\hat{k}_i = \frac{k_i}{k^*}$, $(i = 1, 2, ..., 4)$.

1.2.2 Post-Jump Phase

In order for a jump to be possible, the jumping mechanism must be capable of surpassing the gravitational force once the displacement in the non-linear elastic element has become positive. That is, the restoring force of the non-linear elastic element acting on the lower mass must exceed its weight. The jumping occurs when $\hat{Y}_2 = \hat{Y}_{2,\,jump}$, where:

$$\hat{F}(\hat{Y}_{2,\,jump} - \hat{l}_0) = \hat{G}. \tag{3}$$

The airborne or post-jump phase of the motion is illustrated in Figure 1 (b). Once the bottom mass has left the ground, the governing system of coupled equations of motion can be defined as:

$$\begin{aligned} m\ddot{Y}_1 &= F(Y_2 - Y_1 - l_0) - mg, \\ m\ddot{Y}_2 &= -F(Y_2 - Y_1 - l_0) - mg. \end{aligned} \tag{4}$$

Following the same procedure of section 1.2.1, we can derive the non-dimensional system of equations as follows:

$$\begin{aligned} \frac{d^2\hat{Y}_1}{d\tau^2} &= F(\hat{Y}_2 - \hat{Y}_1 - \hat{l}_0) - \hat{G}, \\ \frac{d^2\hat{Y}_2}{d\tau^2} &= -F(\hat{Y}_2 - \hat{Y}_1 - \hat{l}_0) - \hat{G}. \end{aligned} \tag{5}$$

The initial conditions of equation 5 can be extracted from the solution of pre-jump phase (equation 2). In the next section, we present the numerical simulation results of solving the equations of motion.

1.3 Review of the Effect of Non-Linear Force Displacement Profiles on Jumping Behavior.

Jumping is achieved when the bottom mass loses contact with the ground, as outlined in section 1.2.2. Once the jump begins, the majority of the stored energy in the spring, E_0, is converted to kinetic energy of the upper and lower masses while some is converted to gravitational potential energy as the structure gains altitude. For the sake of the theoretical model, the mechanism is assumed to be subject only to conservative forces and therefore no damping is included. The total energy of the system during the post jump phase is a combination of the kinetic energy of the masses, the gravitational potential energy, and the spring potential energy will be conserved. Due to the non-linear spring element it is expected that the two masses will exhibit unique behaviors during the post jump phase. To this end, we study the response of both masses individually as well as the location of the combined center of gravity to obtain a clear understanding of the dynamic behavior of the system. We begin this investigation by studying the effect of stored elastic energy on the outcome of jumping performance. The stored energy relates to the compression section (negative displacement) of the force-displacement curve. To do so we must first gain an accurate understanding of the principles that govern the relation between the compression section of the force-displacement curve and the jumping behavior of the system (section

1.3.1). However, the tension section of the force-displacement (positive displacement) will also affect the point at which jumping actually occurs, as the bottom mass will not lose contact with the ground until the tension in the spring element equates to the weight of the bottom mass. Therefore, we also investigate the effect of the tension region on overall jumping performance (section 1.3.2).

1.3.1 Energy Storage in the Compressed Region of the force Displacement Curve

The energy storage of the system is shown in Figure 3 (b) is achieved by compressing the spring element to some initial displacement. The stored energy, E_0, is equivalent to the work (W_{ext}) performed on the spring to compress it.

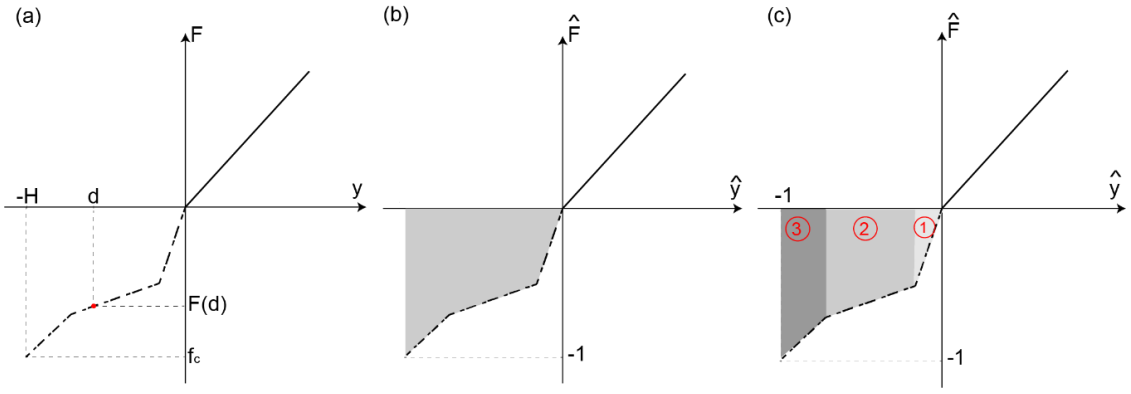

Figure 3: (a) Reaction force-displacement curve of the spring with an initial displacement (d). (b) Non-dimensional force-displacement curve of the spring with the shaded area representing the initial stored energy. (c) Three constituent areas of the shaded region.

The relationship between the stored energy and the reaction force of the spring compressed from the free length can be expressed as:

$$E_0 = W_{ext} = \int_0^d F(y)dy \tag{6}$$

Where d is the displacement from the free length and $F(y)$ is the reaction force in the spring shown in Figure 3 (a). A piecewise linear force-displacement curve is used for representing the non-linear stiffness properties of the system. This section focuses on the general piecewise linear curves that are constrained by the actuation and structural limits shown in Figure 2 (b) to study the effect of non-linear spring elements on jumping performance.

To generalize the energy storage function, equation (6) is non-dimensionalized with respect to the structural and actuation limits of the system.

$$\hat{E}_0 = \int_0^{\hat{d}} \hat{F}(\hat{y}) d\hat{y} \tag{7}$$

where:

$$\hat{E}_0 = \frac{E_0}{\frac{1}{2} k^* H^2}, \hat{d} = \frac{d}{H}$$

The two factors that affect the stored energy are the initial displacement and the force-displacement function. For any given force function, maximum stored energy can be achieved when the spring element is compressed all the way to the structural limit, $\hat{d} = 1$.

The overall shape of the force-displacement curve plays a significant role in the amount of stored energy as well. For a generic piecewise linear force-displacement curve bounded by the structural and actuation limits ($\hat{d} = 1$ and $\hat{F}(d) = 1$ shown in Figure 3 (b)) the stored energy of the system is equivalent to the area between the $\hat{y}$-axis and the $\hat{F}(\hat{y})$ curve, the shaded region in Figure 3 (b). This area can be represented by the summation of three areas, a triangle A_1 and two trapezoids A_2 and A_3.

$$\hat{E}_0 = A_1 + A_2 + A_3 \tag{8}$$

The compression section of the force-displacement curve consists of three piecewise linear curves with three corresponding non-dimensional stiffness coefficients: $\hat{k}_2$, $\hat{k}_3$, and $\hat{k}_4$. The values of these coefficients can be varied independently to affect the total stored energy and therefore the overall jumping performance. By varying the coefficients individually, we can learn about how the overall shape of a non-linear force-displacement curve affects jumping performance.

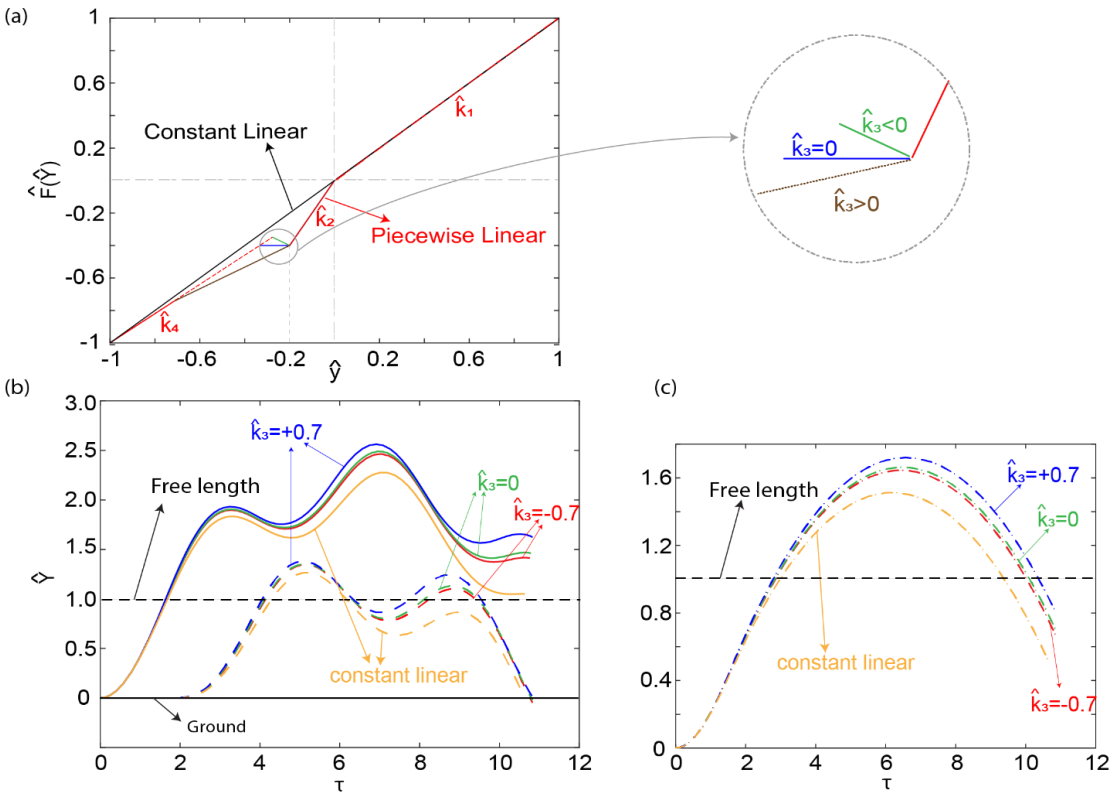

Figure 4: (a) Three different piecewise linear force-displacement curves, with positive, negative and zero 3ˆk stiffness coefficients. (b) Vertical displacement of the upper mass (solid line) and lower mass (dashed line). (c) Vertical displacement of the center of gravity.

Figure 4 (a) show piecewise linear force-displacement curves with a positive, negative, and zero stiffness value for $\hat{k}_3$. A constant linear force-displacement curve would have constant stiffness throughout the entire domain. The largest amount of stored energy from a constant linear stiffness would come from a non-dimensionalized stiffness value $\hat{k} = 1$. We investigate three piecewise linear curves all with the shared values for $\hat{k}_1$, $\hat{k}_2$, and $\hat{k}_4$. The tension stiffness is chosen to match the linear spring, $\hat{k}_1 = \hat{k} = 1$, in order to compare the performance of the non-linear elements in the compression region. Each non-linear curve uses a $\hat{k}_3$ value such that more energy is stored than the linear spring.

MATLAB ODE45 is used to solve the system of ordinary differential equations that governs the structure's motion shown in equation (2). The initial conditions for the upper mass in the pre-jump phase are specified as $[\hat{Y}_2 = 0, \dot{\hat{Y}}_2 = 0]$ where $\hat{Y}_2$ is measured from the ground. The post jump phase of motion defined by equation (5) are extracted from the solution for the pre jump phase once the tension in the spring is large enough to overcome the weight of the bottom mass.

Figure 4 (b) and 4 (c) show the vertical displacement of the center of gravity and the top and bottoms masses individually. The results show that the piecewise linear springs exhibit better jumping performance than the constant linear springs in terms of jumping height (up to 14% better with specified values of $\hat{k}_3$. Jumping performance for the center of gravity and both masses is also better when $\hat{k}_3$ is positive because the mechanisms in this case store more energy due to the greater area between the force-displacement curve and the displacement axis (larger A_2 in Figure 3 (c).)

In addition to jumping height it is also useful to compare energy efficiency of the mechanisms. The higher jumping heights of the piecewise linear springs comes from storing more energy in compression of the system. We define the energy efficiency as the ratio between maximum gravitational potential energy of the center of gravity ($\max(PE_{CG})$) and the initial stored energy (E_0).

$$\eta = \frac{\max(PE_{CG})}{E_0} \times 100\% \tag{9}$$

Figure 5 shows the gravitational potential energies of the three different systems shown in Figure 4. Also in the figure is the initial stored energy of the system with the given initial conditions.

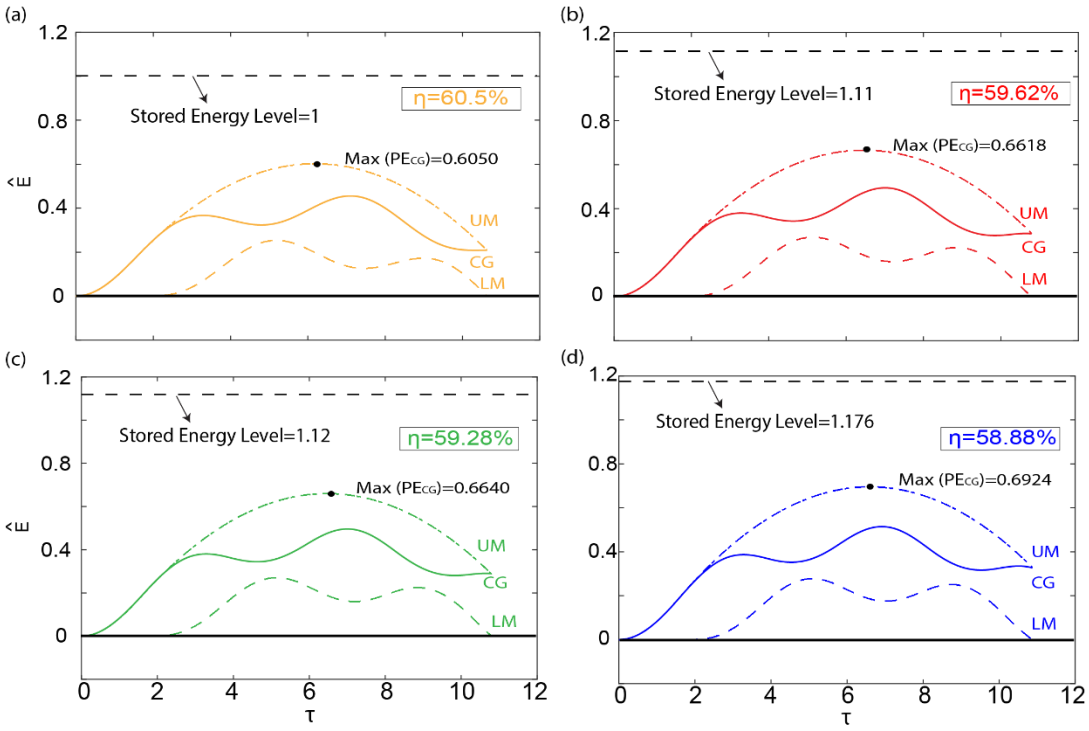

Figure 5: (a) Gravitational potential energy levels of the upper mass (UM), lower mass (LM) and center of gravity (CG) for constant linear stiffness (a); and three piecewise linear cases (b-d). The three piecewise linear force-displacement curves feature the same $\hat{k}_1 = 1, \hat{k}_2 = 2, \hat{k}_4 = 0.9, \hat{y}_c = -0.2$. *But they have different* $\hat{k}_3$ *values: (b)* $\hat{k}_3 = -0.7$, *(c)* $\hat{k}_3 = 0$, *(d)* $\hat{k}_3 = +0.7$.

From the results we can see that the mechanism with piecewise linear springs exhibit a small drop in energy efficiency when compared with the constant linear spring. It is interesting that the piecewise linear spring mechanisms exhibit better jumping performance in terms of jump height while sacrificing energy efficiency. Therefore we further investigate the efficiency drop for the mechanisms with greater initial stored energy. The

initial stored energy for a mechanism with a constant linear spring with stiffness coefficient $\hat{k} = 1$ can be represented by $\hat{E}_0$:

$$\hat{E}_0 = \frac{E_0}{E_{0,linearspring}} = \frac{E_0}{\frac{1}{2}k^* H^2} = 1 + \hat{e} \tag{10}$$

And $\hat{e}$, $(0 \leq \hat{e} \leq 1)$ represents the additional non-dimensional stored energy by utilizing non-linear stiffness properties in the compressions region of the force-displacement curve. The difference between the efficiencies of the nonlinear and linear systems can be represented by the following equation:

$$\Delta\eta = \eta_{linear} - \eta_{non-linear} = \frac{\max(PE_{CG,linear})}{\hat{E}_{0,linear}} - \frac{\max(PE_{CG,non-linear})}{\hat{E}_{0,linear} + \hat{e}} \times 100\% \tag{11}$$

When considering the additional energy due to non-linear spring elements that will be converted into the kinetic energy of the system during the jump it can be shown that:

$$\eta_{linear} - \eta_{non-linear} = \left(2\hat{G}\frac{\hat{e}}{1+\hat{e}} \right) \times 100\% \tag{12}$$

Equation (12) implies that there is a hyperbolic relationship between the efficiency drop of a non-linear mechanism and the additional stored energy $\hat{e}$. The more energy that is stored in the pre-jump phase due to the non-linear behavior of the force-displacement curve, the less efficient the system becomes. It is also important to note that the efficiency

drop is linearly dependent on $\hat{G}$, the ratio between the mass of the jumping mechanism and the reaction force in the spring (the actuation limit of the system). For a typical jumping mechanism, this ratio should be designed to be small, i.e. significantly less than one. For this study, $\hat{G} = 0.1$. As a result of the small value for $\hat{G}$ the magnitude of the efficiency drop from using non-linear springs is also small (less than 2%). In this case, the benefit of better jumping performance (up to 14% increased height of the center of gravity) outweighs the sacrifice in system efficiency.

The results indicate that using non-linear spring elements in a jumping mechanism can significantly increase jumping height and therefore improve jumping performance at a minimal cost of energy efficiency, all while staying within the structural and actuation limits of the system. The results are based on a C^0 piecewise linear force-displacement curve, but the principles can be directly extended to any C^n $(n \geq 1)$ nonlinear curves.

1.3.4 Tensile Region of the Force-Displacement Curve and its Effect on Internal Oscillation in the Post-Jump Phase

The previous section analyzes the effect of using non-linear properties to increase energy storage in the compression region of the force displacement curve. However, to fully comprehend the effect of nonlinear springs on jumping behavior the tension region (positive displacement) must be studied as well. The values for $\hat{k}_2$ and $\hat{k}_4$ are the same as in the previous section while $\hat{k}_3 = +0.7$. To study the effects of the tensile region, the values for $\hat{k}_1$ will differ. Three values are chosen; $\hat{k}_1 = 1$ will have the same stiffness as the constant linear spring previously discussed, while $\hat{k}_1 = 0.5$ and $\hat{k}_1 = 5$ represent

springs with softer and stiffer tension stiffness with respect to the constant linear spring. The shape of the force displacement curve with varying values for $\hat{k}_1$ is shown in Figure 6.

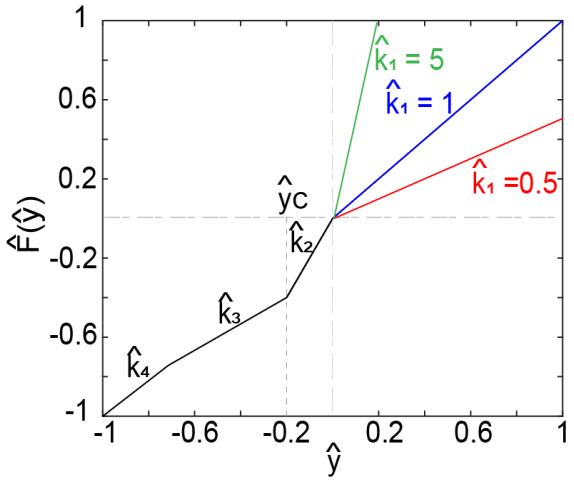

Figure 6: Three different piecewise linear force-displacement curves with the same compression section ($\hat{k}_2 = 2, \hat{k}_3 = +0.7, \hat{k}_4 = 0.9, \hat{y}_c = -0.2$) but different tension stiffness coefficients.

Figure 7 (a) shows the jump height of both masses based on the different stiffness values in the tensile region. From Figure 7 (c) it can be seen that changing the stiffness of the tensile region does not affect the maximum height achieved by the center of gravity. However, the tensile stiffness does affect the internal oscillations within the mechanism within the post jump phase. Form Figure 7 (b) we can observe that increasing the tension stiffness decreases the magnitudes of the oscillations between the upper and lower masses but increases the frequency.

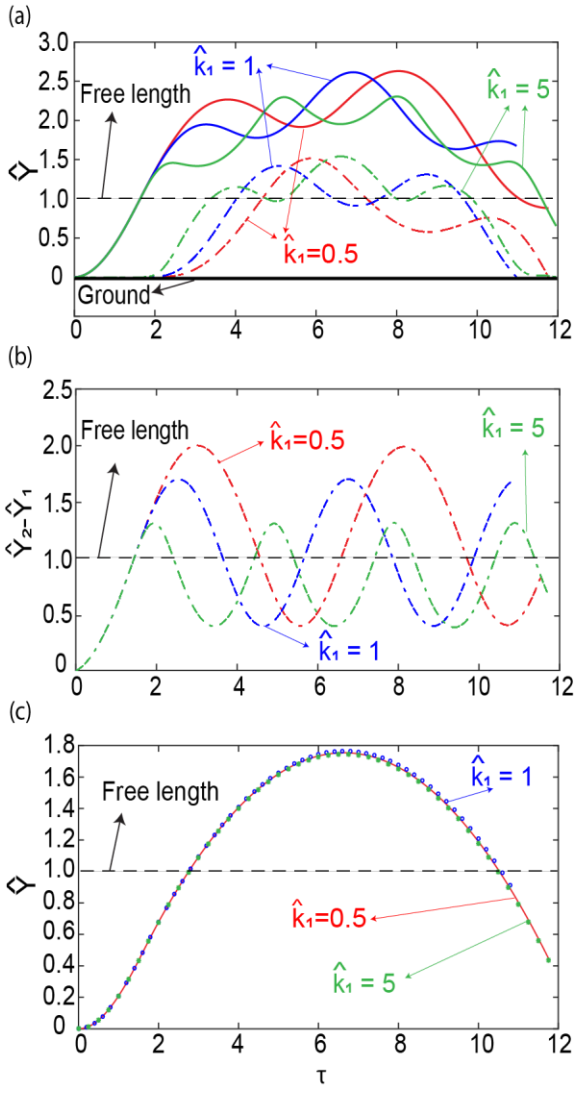

Figure 7: (a) Vertical displacement of the upper mass (solid line) and the lower mass (dashed line). (b) Internal oscillations of the jumping mechanism. (c) Vertical displacement of the center of gravity. Colors are the same as in figure 6.

To better understand the effects the tension stiffness has on the oscillations between the masses we will perform a modal analysis on the system. Figure 1 (b) shows the post-jump phase of motion while the system is airborne. The equations of motion in this phase

with equal top and bottom mass is given by equation (5). Given a more general case where the top and bottom masses are different the system can be defined as follows:

$$\begin{aligned} m_1\ddot{z}_1 &= F(z_2 - z_1) - m_1 g \\ m_2\ddot{z}_2 &= -F(z_2 - z_1) - m_2 g \end{aligned} \tag{13}$$

Where z_1 and z_2 are measured from the ground and the free length respectively, and $F(z_2 - z_1)$ is a nonlinear function. During the oscillations, the system is simplified to use only the tension stiffness k_1 to represent the stiffness characteristics around the equilibrium position ($z_2 = 0$). The post jump phase of motion initially begins when the spring is under tension and that is why we make this assumption. The equations of motion can then simplify into linear matrix form:

$$\begin{aligned} \begin{pmatrix} \ddot{z}_1 \\ \ddot{z}_2 \end{pmatrix} &= \begin{pmatrix} \frac{-k_1}{m_1} & \frac{k_1}{m_1} \\ \frac{k_1}{m_2} & \frac{k_1}{m_2} \end{pmatrix} \begin{pmatrix} z_1 \\ z_2 \end{pmatrix} + \begin{pmatrix} -g \\ -g \end{pmatrix} \leftrightarrow \underline{\ddot{Z}} \\ &= [K]\underline{Z} - \underline{g} \end{aligned} \tag{14}$$

With the matrix form, we can then solve for the eigenvalues and eigenvectors of the stiffness matrix $[K]$ by:

$$\begin{aligned} \lambda_1 = 0, v_1 &= \begin{pmatrix} 0 \\ 0 \end{pmatrix} \\ \lambda_2 = -k_1 \frac{m_1 + m_2}{m_2 m_2}, v_2 &= \begin{pmatrix} -\frac{m_2}{m_1} \\ 1 \end{pmatrix} \end{aligned} \tag{15}$$

It can be shown with diagonalization:

$$[K] = [V][\Lambda][V]^{-1} \tag{16}$$

Where:

$$[V] = (\underline{v_1} \quad \underline{v_2}) = \begin{pmatrix} 1 & -\frac{m_2}{m_1} \\ 1 & 1 \end{pmatrix}$$
$$[\Lambda] = \begin{pmatrix} \lambda_1 & 0 \\ 0 & \lambda_2 \end{pmatrix} = \begin{pmatrix} 0 & 0 \\ 0 & -k_1 \frac{m_1 + m_2}{m_1 m_2} \end{pmatrix} \tag{17}$$

So therefore equation (14) can be updated as follows:

$$\underline{\ddot{Z}} = [V][\Lambda][V]^{-1}\underline{Z} - \underline{g} \tag{18}$$

And multiplying both sides of equation (18) by V^{-1}:

$$[V]^{-1}\underline{\ddot{Z}} = [\Lambda][V]^{-1}\underline{Z} - [V]^{-1}\underline{g} \tag{19}$$

And defining $\underline{U} = [V]^{-1}\underline{Z}$ such that:

$$\underline{U} = \begin{pmatrix} u_1 \\ u_2 \end{pmatrix} = [V]^{-1}\underline{Z} = \begin{pmatrix} \frac{m_1 z_1 + m_2 z_2}{m_1 + m_2} \\ \frac{m_1}{m_1 + m_2}(z_2 - z_1) \end{pmatrix} \tag{20}$$

From equation (20) we can see that u_1 represents the position of the center of gravity and u_2 represents the magnitude of the internal oscillatory motion. Now using $\underline{U}$ as the new state variable, equation (18) becomes:

$$\underline{\ddot{U}} = [\Lambda]\underline{U} - [V]^{-1}\underline{g} \tag{21}$$

And by substituting $[\Lambda]$ and $[V]^{-1}$ matrices into equation (21) we obtain:

$$\begin{pmatrix}\ddot{u}_1\\ \ddot{u}_2\end{pmatrix} = \begin{pmatrix}0 & 0\\ 0 & -k_1\dfrac{m_1+m_2}{m_1m_2}\end{pmatrix}\begin{pmatrix}u_1\\ u_2\end{pmatrix} - \begin{pmatrix}\dfrac{m_1}{m_1+m_2} & \dfrac{m_2}{m_1+m_2}\\ -\dfrac{m_1}{m_1+m_2} & \dfrac{m_1}{m_1+m_2}\end{pmatrix}\begin{pmatrix}g\\ g\end{pmatrix} \tag{22}$$

Which yields the two equations:

$$\ddot{u}_1 = -g\left(\frac{m_1}{m_1+m_2}+\frac{m_2}{m_1+m_2}\right) = -g$$
$$\ddot{u}_2 = -k\left(\frac{m_1+m_2}{m_1m_2}\right)u_2 \tag{23}$$

Clearly the acceleration of the center of gravity is independent of the stiffness in the tension section of the mechanism and is always equal to $-g$. From this we can conclude that even with different stiffness coefficients in the tension region the center of gravity movement will always remain the same, provided the system has the same initial stored energy, which can also be observed in Figure 7 (c). The frequency of the internal oscillations of the simplified mechanism can be found by:

$$\Omega = \sqrt{\frac{m_1+m_2}{m_1m_2}k_1} \tag{24}$$

Although this frequency is only for the simplified mechanism and not the nonlinear system. However, it does suggest that the frequency is dependent on tension stiffness for the mechanism which agrees with the observations we can make from Figure 7 (b) which shows numerical simulation results of the nonlinear system.

From this we can deduce that changing the stiffness coefficient of the tension region does not affect the jumping behavior of the center of mass, it does affect the internal oscillations and therefore could affect the maximum reach or clearance of the mechanism.

CHAPTER TWO

USING THE TACHI-MIURA POLYHEDRON (TMP) BELLOWS TO ACHIEVE NON-LINEAR FORCE DISPLACEMENT BEHAVIOR

In the previous section I outlined how non-linear stiffness characteristics can improve the performance of a generic jumping mechanism. Achieving non-linearity in practice however can be challenging for engineers as most springs and elastic elements readily available for design exhibit linear stiffness properties. In the following sections, I show how it is possible to use rigid foldable origami structures to obtain non-linear stiffness properties, specifically a Tachi-Miura Polyhedron (TMP) bellows developed by Yasuada, Tachi, and Yang [36]. From there, I use a genetic algorithm to optimize the design of the TMP Bellows structure to have the best theoretical jumping performance based on numerical simulations within a set of provided design constraints. The results from the optimization for the design parameters can then be used directly to manufacture a TMP Bellows with an optimum force-displacement profile. This work has already been published and discussed in [40] and the figures come from that paper.

2.1 Defining the Geometry and Force Displacement Profile of the TMP Bellows

The TMP bellow is essentially a linear assembly of identical unit cells and each cell consists of two connected origami sheets (aka. the front sheet and back sheet shown in Figure 8 (a,b)). The geometric design of two origami sheets can be uniquely defined based on two fold lines (l, m), the side length (d), and a sector angle (α). For clarity, we refer

the fold lines that remain parallel to the horizontal *x*-*z* reference plane as the "main-folds" and all other fold lines are the "sub-folds" (Figure 8 (b)).

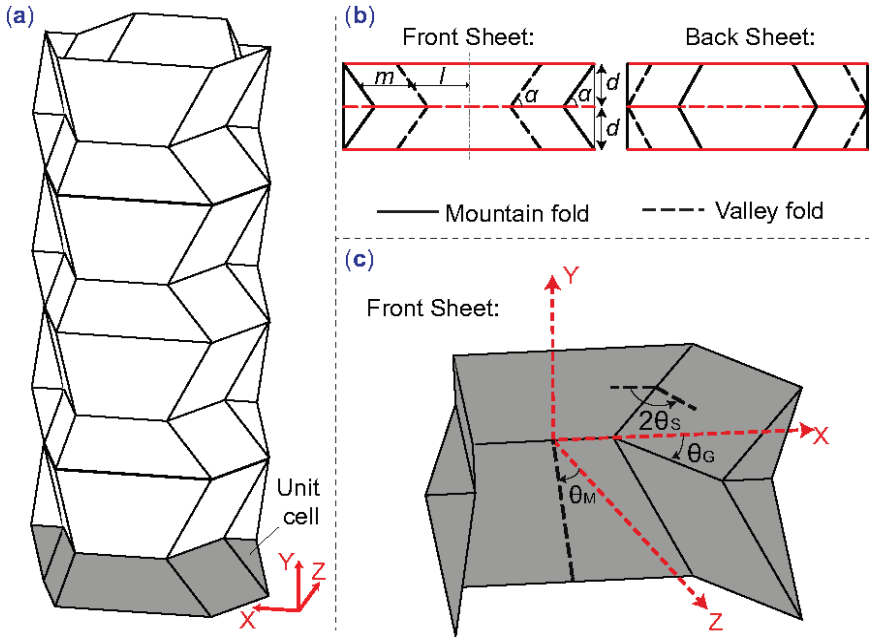

Figure 8: Design of the Tachi-Miura Polyhedron (TMP) bellow. (a) The overall external geometry of a TMP bellow; this one consists of eight unit cells, and one of them is highlighted in gray. (b) The crease design of the front sheet and back sheet that makes up two unit cells. The main-folds are highlighted by red color. (c) The external geometry of a folded front sheet, showing the different angles used in the kinematics and mechanics analysis.

Despite the relatively complex geometry, TMP bellow is *rigid-foldable* in that its folding motion does not induce any deformations in the facets. Therefore, we can assume the facets are rigid, and the fold lines behave like perfect hinges with assigned torsional stiffness. In this way, we can use the virtual work principle and estimate the reaction force F of the TMP bellow along its length direction (*y*-axis in Figure 8 (a)) as follows,

$$F = \frac{-32}{Nd\cos\theta_M}\Big[k_M(N-1)\left(\theta_M-\theta_{M_0}\right)+\ldots \\ Nk_S\left(\theta_S-\theta_{S_0}\right)\frac{\cos^3\theta_G/2\sin\theta_M}{\cos\alpha\sin\theta_S}\Big]. \tag{25}$$

In this equation, N is the number of unit cells in the TMP bellow; k_M and k_S are the equivalent torsional stiffness of the main-folds and sub-folds, respectively; θ_M is the dihedral angle associated with the main-folds, defined between the facets and *x*-*z* reference plane as shown in Figure 8 (c); θ_S is the dihedral angle between the facets along the sub-folds; and θ_S is the angle between *x*-axis and a main-fold. Denote u as the change in unit cell height through folding and θ_{M0} as the main fold angle corresponding to the initial, resting configuration, the magnitude of these angles can be calculated as

$$\theta_M = \sin^{-1}\left(\sin\theta_{M0}-\frac{u}{Nd}\right), \tag{26}$$

$$\theta_G = 2\tan^{-1}\left(\tan\alpha\cos\theta_M\right), \tag{27}$$

$$\theta_S = \cos^{-1}\left(\frac{\sin\frac{\theta_G}{2}}{\sin\alpha}\right). \tag{28}$$

Figure 9 (a) illustrates the force displacement curve of a TMP bellow design based on $l=m=d=30\text{mm}$, $\alpha=40°$, $\theta_{M0}=65°$, and $k_M=k_S=0.03\,\text{N.m}/rad$. Due to the nonlinear geometric relationships induced by origami folding, the TMP bellow shows a strong nonlinearity. In particular, it shows a "strain softening" behavior in compression.

That is, the TMP exhibits a high stiffness under small compressive deformation, but its stiffness decreases as the deformation increases.

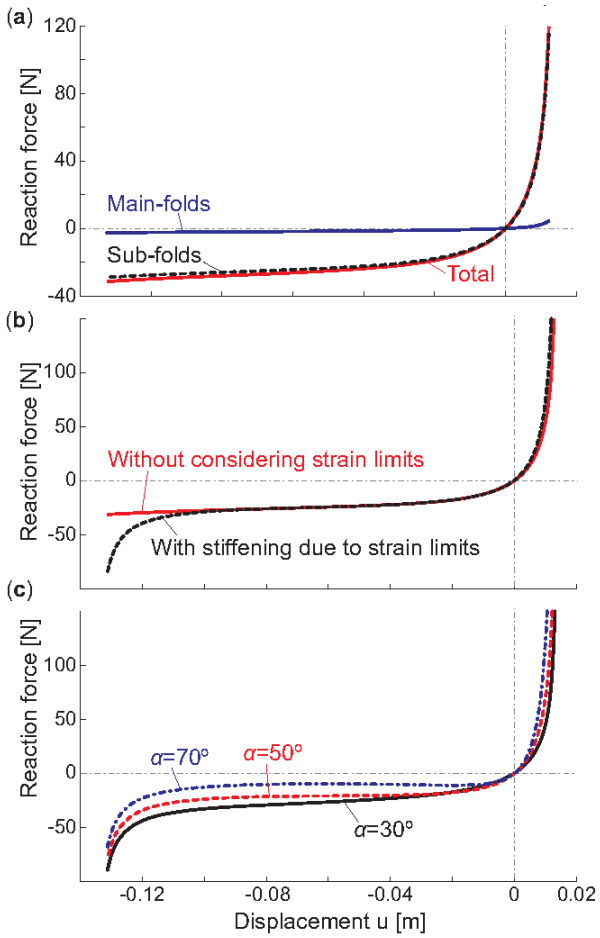

Figure 9: The force-displacement curve of a TMP bellow. (a) The contribution of main-folds and sub-folds to the overall reaction force, and the sub-folds show the desired "strain softening" behavior in compression. (b) The modified reaction force curve considering the deformation limit due to folding. (c) The reaction force curve corresponding to different α angles, while all other design variables remain the same as those used in (a).

As outlined in Section 1.3.1, such nonlinearity is desired because it can store more energy upon compression compared to the traditional linear spring, leading to a higher jump. Moreover, after careful examinations, I discover that the reaction force generated

by the sub-folds shows a stronger nonlinearity than the main-folds. Therefore, I will intentionally weaken main-folds and stiffen up the sub-folds to strengthen the desired non-linearity. This allows us to neglect the contribution of the main-folds to the overall reaction force, and simplify equation (25) into the following:

$$F = \frac{-32k_S}{Nd\cos\theta_M}\left[N\left(\theta_S - \theta_{S0}\right)\frac{\cos^3\frac{\theta_G}{2}\sin\theta_M}{\cos\alpha\sin\theta_S}\right]. \tag{29}$$

However, this reaction force equation does not consider the deformation limits due to rigid folding. That is, TMP bellow can only be folded in-between its compression limit at $\theta_S = 0°$ (fully compressed) and extension limit at $\theta_S = 90°$ (fully stretched). However, in reality when the TMP is compressed near $\theta_S = 0°,$ its facets would come into contact with each other and resist further compression. On the other hand, when the TMP is extended near $\theta_S = 90°,$ both the front and back sheets are stretched flat so that the overall tension stiffness would increase significantly. To incorporate these deformation limits by folding, I adopt the method developed by Liu and Paulino [41] and set two folding angle limits: $\theta_1 = 20°$ for compression and $\theta_2 = 70°$ for tension. When $\theta_S < \theta_1,$ the reaction force equation (29) is modified into the following:

$$\begin{aligned} F = \quad & \frac{-32k_S}{Nd\cos\theta_M}[N(\theta_1 - \theta_{S0}) + ... \\ & \frac{2\theta_1}{\pi}\tan\left(\frac{\pi(\theta_S - \theta_1)}{2\theta_1}\right)\frac{\cos^3\frac{\theta_G}{2}\sin\theta_M}{\cos\alpha\sin\theta_S}]. \end{aligned} \tag{30}$$

Similarly, when $\theta_S > \theta_2,$ the reaction force becomes,

$$F = \frac{-32k_S}{Nd\cos\theta_M}[N(\theta_2 - \theta_{S_0}) + ... \\ \frac{2\theta_2}{\pi}\tan(\frac{\pi(\theta_S - \theta_2)}{2\theta_2})\frac{\cos^3\frac{\theta_G}{2}\sin\theta_M}{\cos\alpha\sin\theta_S}] \quad (31)$$

Figure 9 (b) illustrates the modified reaction force, which is used for the subsequent dynamic analysis and optimization. Figure 9 (c) illustrates the effect of the sector angle α on the force-displacement curve. When other design variables are fixed, increasing the α angle would decrease the reaction force in the structure when compressed. This leads to less stored strain energy. For this reason I would expect smaller alpha angles to lead to better jumping performance.

2.2 Optimizing the TMP Bellows Design for Improved Jumping Performance

The goal of this optimization is to identify the TMP bellow design that can lead to the best jumping performance. To this end, I describe the jumping performance based on two different objectives: Airtime and Clearance (illustrated in Figure 10). Airtime is the total time that the jumping mechanism spends in the air; and Clearance is the peak height achieved by the lower mass. I normalize the Clearance by the rest height of TMP bellow and use the normalized values as the optimization objective function.

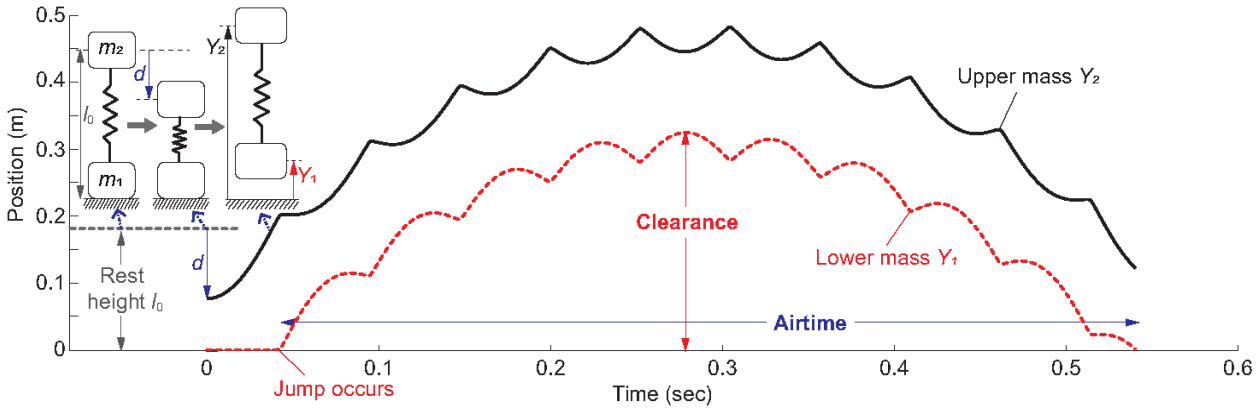

Figure 10: A typical time response of the TMP origami jumper. The schematic plots at the upper left corner illustrates the origami jumper at resting configuration, initial configuration when the upper mass is compressed, and post jump phase, respectively. The two objective functions of the design optimization: Airtime and Clearance are highlighted. Notice the internal oscillation during the post jump phase influences the Clearance performance.

There are five design variables that that can be tailored to optimize the jumping performance. The definition and range of these variables are listed in Table 1, and Figure 8 illustrates how they relate to the overall geometry of TMP bellow. Moreover, three geometric constraints are imposed. The first constraint ensures that the design of TMP bellow is properly defined and there are no conflicting crease lines. The second constraint defines a minimum main-fold length for the ease of manufacturing and assembly. The third constraint sets an upper limit on the unit cell length. The additional 15mm in the third constraint is for an extended tab to facilitate the assembly of two sheets.

Table 1: The design variables and geometric constraints used in the design optimization

N: Unit cell #	$4 \le N \le 10$
d: Side length	$20\text{mm} \le d \le 40\text{mm}$
α: Sector angle	$30^\circ \le \alpha \le 70^\circ$
l: Fold length	$20\text{mm} \le l \le 40\text{mm}$
m: Fold length	$20\text{mm} \le m \le 40\text{mm}$
Constraint 1:	$2l - d\cot\alpha + 2m\cos\alpha \ge 0$
Constraint 2:	$\frac{d}{2\tan\alpha} - l \le -10\text{mm}$
Constraint 3:	$2\left(l + m + \frac{d}{2}\tan\left(\frac{\pi}{2} - \alpha\right) + 15\right) \le 300\text{mm}$

In this study, the three constraints on design variables are defined based on the fabrication capabilities available to the author. Increasing the variables beyond the upper limits would require additional fabrication equipment; while reducing them below the lower limit would makes assembly too difficult. Regardless, we can still obtain valuable insights on the correlations between the design variables and jumping performance within these constraints.

Table 2: Other design variables used in the optimization.

M : End masses	$m_1 = m_2 = M = 0.25\text{kg}$
θ_{M_0} : Resting main-fold angle	$\theta_{M_0} = 65^\circ$
FR : Initial folding ratio	$FR = \frac{90° - \theta_M}{90^\circ} \times 100\% = 75\%$
k_S : Sub-fold stiffness	$k_S = 0.0383\, N.m/rad$

Besides the geometric design variables of TMP bellow, the magnitudes of some other variables are defined for the optimization (Table 2). One of them is the stress-free, resting folding angle of the main-folds θ_{M0}. However, a very large resting folding angle is difficult to achieve in experiments. Based on repeated trial-and-errors using TMP prototypes of different geometric designs, $\theta_{M0} = 65^\circ$ is found to be a realistic value. Another important variable is the initial folding ratio, which is essentially the initial condition of the dynamic simulation discussed below. Again, after repeated trial-and-error, it is found that an initial folding ratio of 75% is preferred because it can achieve the maximum stored energy for jumping without inducing any significant plastic deformation. The crease torsional stiffness coefficient *k* is estimated based on the experimental data gathered from different shim stock, which will be used to stiffen the sub-folds.

I numerically simulate the jumping behavior of the TMP mechanism in MATLAB using ode45 solver for the different jumping phases outlined in section 1.2.1 and 1.2.2. In these simulations, I assume the upper mass is lowered so that the TMP bellow is compressed to the initial folding ratio of 75%, and then the upper mass is released for jumping. I then use the ode45 solver to obtain the pre-jump time response according to equations (29, 30, and 31). Based on this response, I can identify the moment when the TMP bellow is stretched to the point that its resulting tension force surpass the weight of lower mass. At this moment, the lower mass leaves the ground so that we can use this as the initial conditions for the post-jump phase. Ode45 solver is used again to obtain the time response of the jumping phase so that the Airtime and Clearance can be recorded. To optimize the TMP bellow design, I integrate the jumping simulations and ModeFrontier using the NSGA-II optimization algorithm. NSGA-II is a common genetic algorithm for multi-objective optimization problems. I use a total population size of 2500 individuals across 5 generations. Interested readers can refer to [42] for a complete description of this optimization method. The optimization results according to each objective function are represented in Table 3.

Table 3: Optimized TMP Bellows designs for Airtime and Clearance Objectives

	N	**α** [°]	**d** [mm]	**l** [mm]	**m** [mm]	Airtime [sec]	Normalized Clearance
Airtime Optimum	10	30	20	28.5	20	0.502	179%
Clearance Optimum	4	30	20	28.5	20	0.320	183%

From the results in Table 3, one can observe that the optimized sector angle α is always at its lower limit. As I explained in Section 4.1, a lower α angle corresponds to a stronger nonlinearity in the force-displacement relationship of the TMP bellow (Figure 9 (c)), which is desired for better jumping performance. The optimized unit cell side length *d* and the crease length *l*, *m* are the same. Moreover, *d* and *m* are also at their lower limit. The unit-cell side length *d* appears in the denominator of the reaction force equation (29), so a small side length corresponds to a bigger reaction force and therefore more stored strain energy for jumping. The crease length *m* does not appear in the reaction force equation explicitly, but its value is kept low to avoid violating the third geometric constraint. Similarly, the value of crease length *l* is also kept low to avoid violating the second geometric constraint.

The difference between the two optimized designs are the number of unit cells *N*. More unit cells in a TMP bellow means a larger initial displacement of the upper mass, therefore more strain energy is stored for jumping and a longer airtime. However, increasing the *N* values also increases overall structure height, which can negate the performance of normalized Clearance. Such a trade-off between Airtime and Clearance can be illustrated in the Pareto front shown in Figure 11.

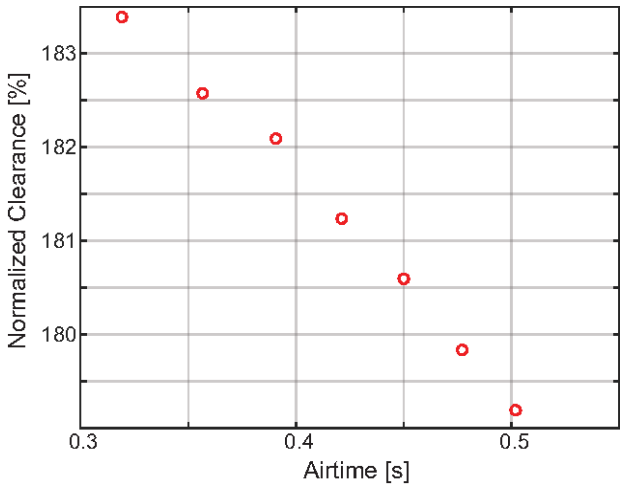

Figure 11: Pareto front obtained in the optimization results

CHAPTER THREE

EXPERIMENTAL CONFIRMATION OF NON-LINEAR FORCE DISPLACEMENT PROFILE IN THE TMP BELLOWS

From the results of the optimization procedure in the previous section I obtain design specifications for the TMP bellows. I use the design parameters to manufacture the TMP bellows for both the original design and the optimized design for maximum clearance from the parameters outlined in section 2.2. I then subject the TMP structures to compression tests to measure the response of their force-displacement curves and compare them to that of the theoretical models. For both the original and the optimized designs we are able to obtain greater than 90% agreement between the predicted force-displacement profile based on equations (29, 30 and 31) and the experimental data. Additionally, I am able to confirm up to a 75% increase in stored energy of the system for the optimized design over the original design that directly leads to improved jumping performance.

3.1 Manufacturing of the TMP and Crease-line Modifications and their Effect on Torsional Fold Stiffness

To confirm the performance of the TMP bellows it had to be manufactured and folded based on the design variables outlined in section 2.2. Initial prototypes of the TMP were made out of paper, with perforations along the crease lines to encourage proper folding. An example of a TMP made from paper can be seen in Figure 16. Manufacturing the TMP out of paper first provided valuable insight on the best techniques for assembly. However,

the torsional stiffness of the creases when the structure is made from paper are not large enough to generate enough force to exhibit jumping.

Flexible plastic sheets are able to be folded similar to paper while maintaining a considerably larger torsional stiffness along the creases. For this reason, along with its availability, polypropylene sheets of 0.5mm thickness are used to assemble the TMP structure.

As discussed in Chapter Two the majority of the non-linear behavior of the force displacement curve of the TMP bellows comes from the sub-folds. In the optimization, the sub-folds were stiffened, and the main folds weakened with sufficient magnitude to neglect the main folds in the calculations. In order to achieve this in practice, the groove-joint compliant hinge researched by Delimont, Magelby, and Howell [43] is implemented into the design. It was found that cutting a groove halfway through the material on a "valley" fold actually strengthens the fold by allowing for more bending behavior along the crease rather than pure stretching and deformation of the material. Conversely, applying the same groove on a mountain fold weakens the crease line and it behaves more like an ideal hinge. The mountain and valley folds for the TMP are outlined in Figure 8 (b). The benefit of applying the groove-joint is threefold. The groove joint allows us to strengthen the sub folds by scouring their valleys, weaken the main folds by scouring their mountains, and the grooves encourage proper folding behavior of the material by establishing the perfect crease lines of the design.

The manufacturing process begins by drawing a single unit cell in Solidworks based on the values for the design parameters outlined in Figure 8. There will be 4 drawings for

each TMP structure, one for each side of the front and back sheet of the TMP. Each drawing contains the crease lines that need to be grooved to either strengthen or weaken the fold. Additionally, note the stress relief holes at the vertices of the crease lines. Removing the material at the vertices allows proper folding of the structure by removing the points of critical stress to prevent buckling. The Solidworks model for one side of the back sheet is shown in Figure 12.

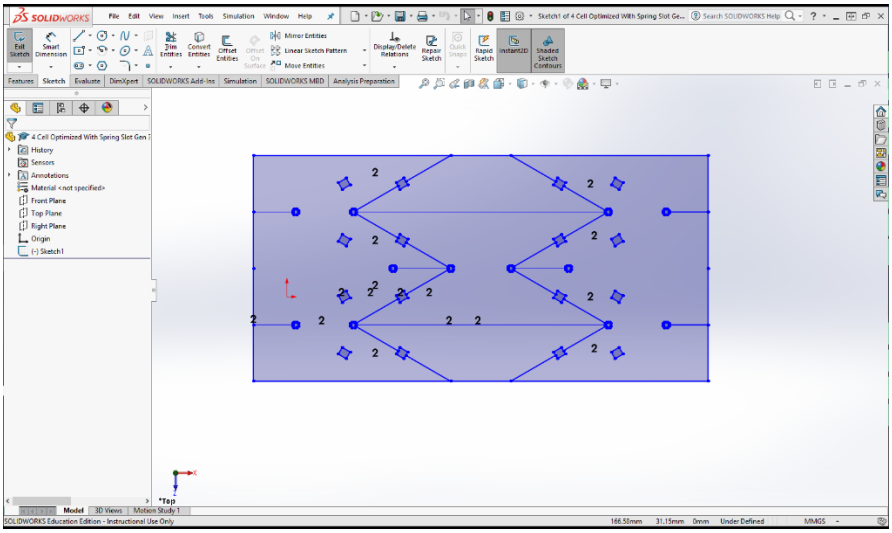

Figure 12: Solidworks Model of the Back Side Crease Lines for one of the 2 Sheets Necessary for the TMP Bellows. Dimensions are Based on the Design for Optimized Clearance

After the model is created in Solidworks it is converted into an adobe illustrator file. Doing so allows each line to be categorized into one of three different layers. The layers define if the material only needs to be grooved or through cut and also specifies which order to cut the lines in. and Adobe Illustrator file for one side of the back sheet of the TMP is shown in Figure 13.

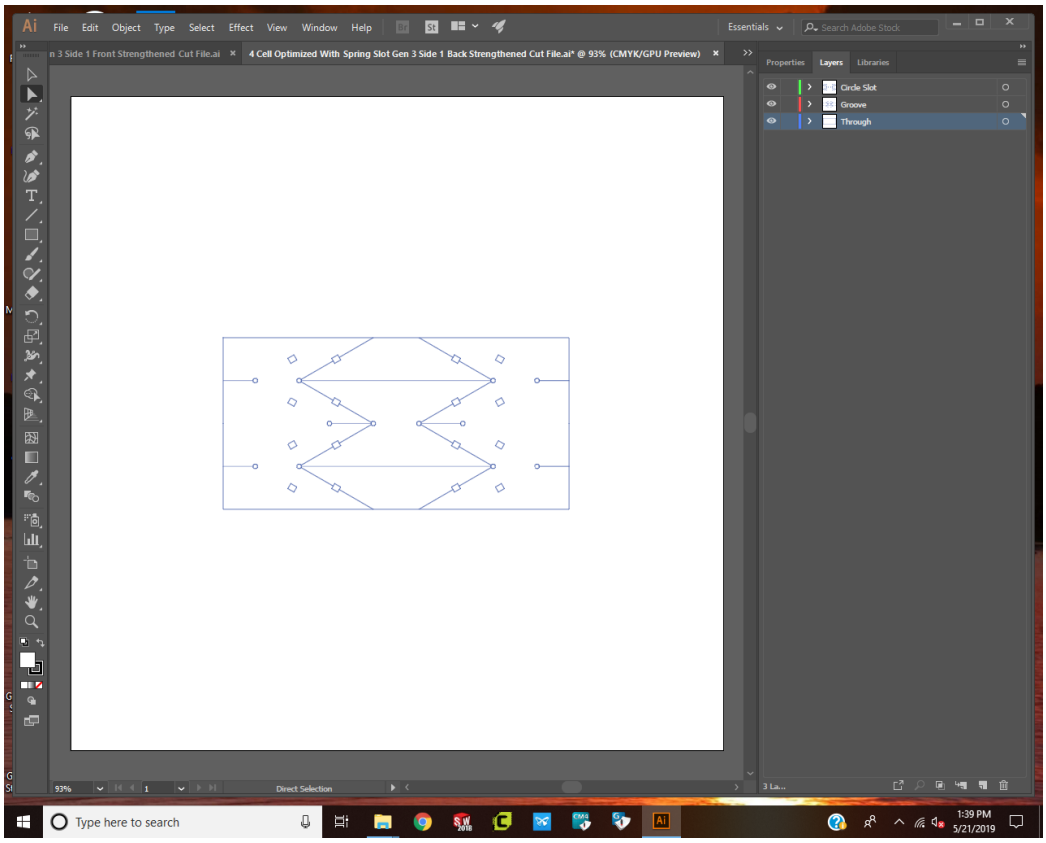

Figure 13:Adobe Illustrator file for the Back Side Crease Lines for one of the 2 Sheets Necessary for the TMP Bellows. Dimensions are Based on the Design for Optimized Clearance

The adobe illustrator file can then be uploaded to the Graphtec FCX4000-50ES Cutter used to cut the crease lines into the polypropylene sheets. Specifications for the FCX4000 can be found in Appendix A. When cutting the sheets, extreme care must be taken to align the material properly based on which side of the front or back sheet is being cut. As previously stated, it is desired to increase the stiffness of the sub folds by applying a groove on the valleys while decreasing the main fold stiffness by applying a groove on the mountains. This means that after grooving and cutting the strain reliefs for one side of the front or back sheet, the same material must be flipped over and aligned on the cutter such that the grooves and cuts for the reverse side are aligned appropriately with those already

made. Grooves and cuts being made on the reverse side of one of the sheets can be seen in Figure 14.

Figure 14: The FCX4000 Cutter In progress Cutting the Grooves and Stress Reliefs for one of the Necessary Sheets for the TMP Bellows

After the cutter has applied the grooves to the crease lines and through cut the border and the stress reliefs, I obtain a flat sheet as shown in Figure 15. From here, the stress reliefs are pushed out and the sheet is folded along the grooved crease lines into the shape of the TMP structure.

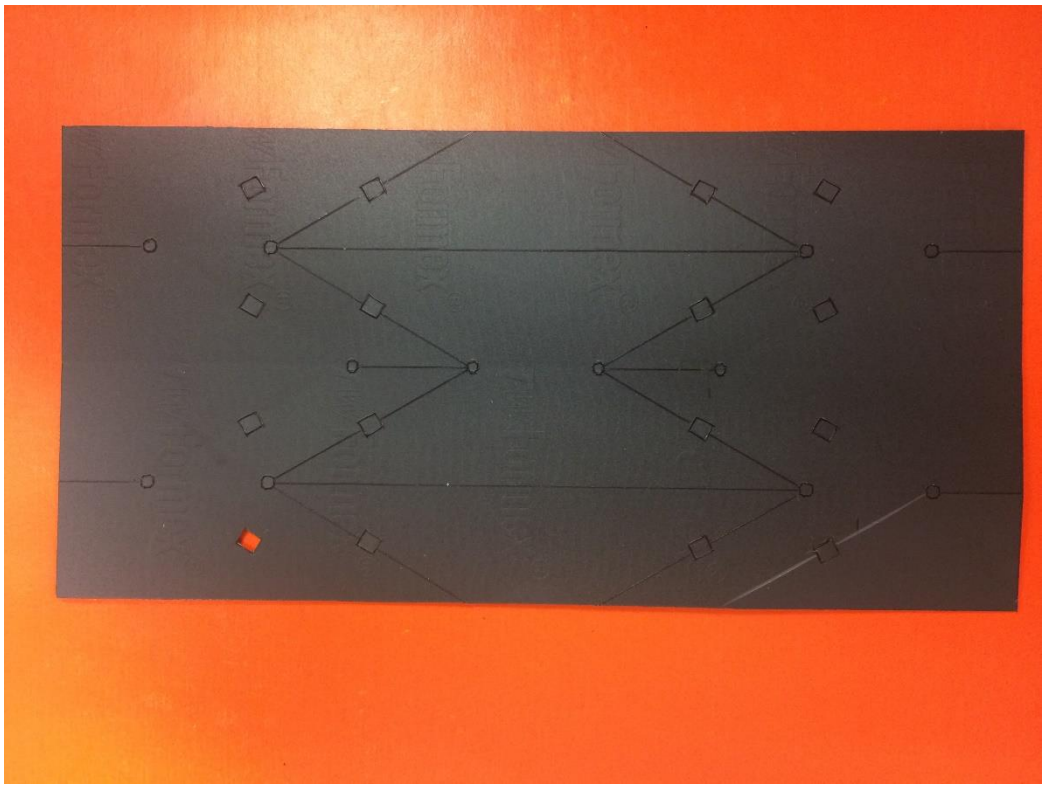

Figure 15: The back side of one Sheet Necessary for the TMP before folding

After both sheets have been folded into the proper shape, they are stapled together along the end faces outside of the crease lines at each unit cell. Fully assembled TMP Bellows structures are shown in Figure 16, Figure 17, and Figure 18.

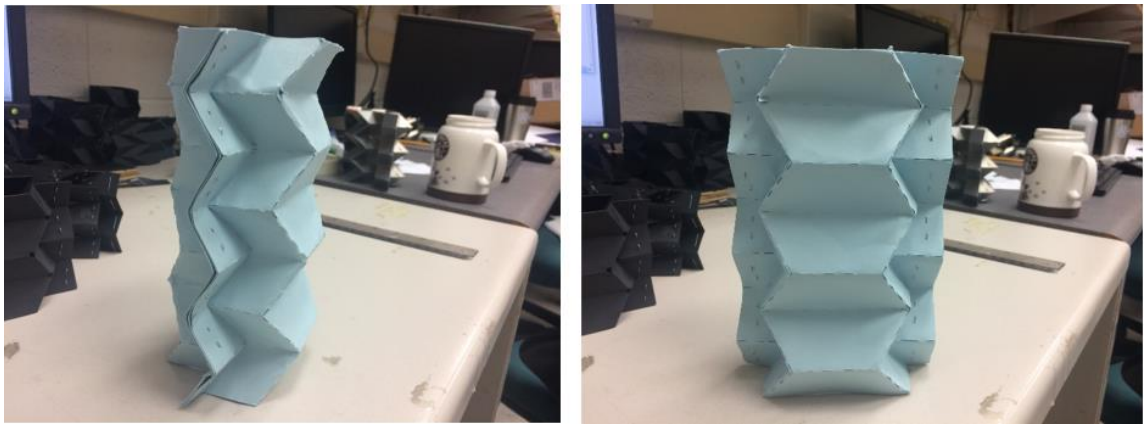

Figure 16: TMP Bellows Manufactured from Paper

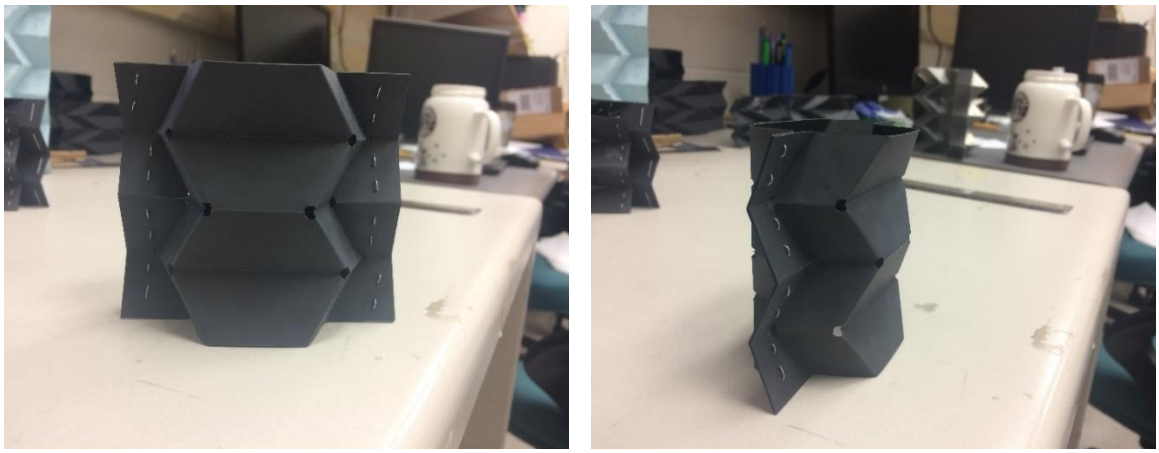

Figure 17: Original TMP Bellows Design Manufactured from Polypropylene

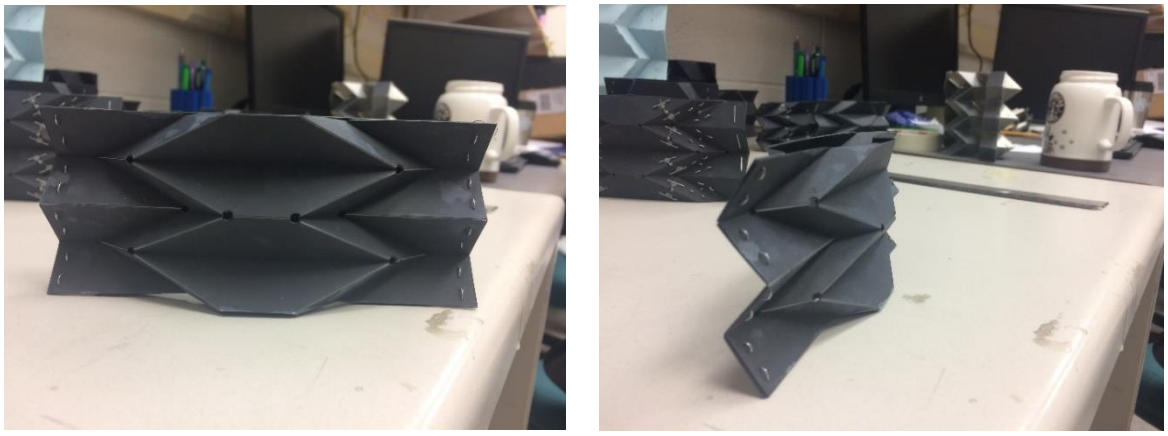

Figure 18: Optimized TMP Bellows Design Manufactured from Polypropylene

After assembling the TMP structure from polypropylene sheets it can be observed that the force required to compress down to its desired initial folding ratio is up to eight times more than that of the force required to compress the paper structure. However, the exact value for torsional stiffness of the creases must be backwards calculated from experimental data. I use an ADMET Expert 5601 Displacement controlled Tensile testing machine (specifications shown in Appendix B) with a calibrated load cell to measure the force-displacement response of the TMP. The testing system compresses the TMP to a set limit while continuously measuring the force applied back to the load cell. The displacement limit is determined based on the 75% folding ratio as the initial condition defined in section 2.2. Figure 19 shows the setup of the machine for the TMP compression tests.

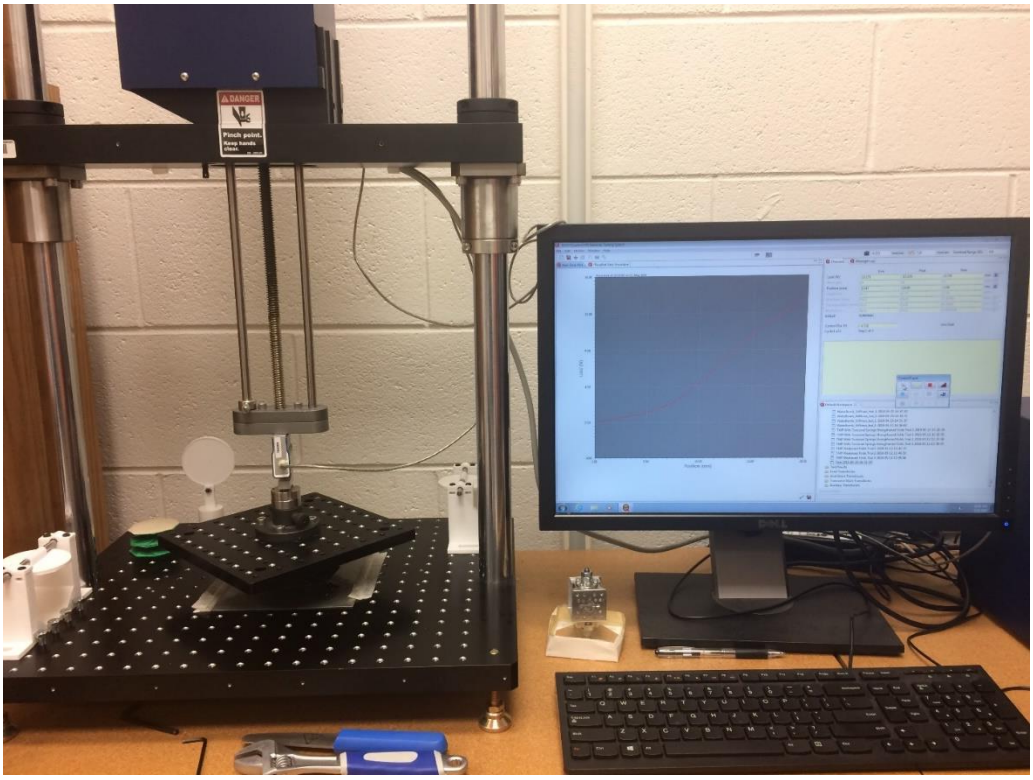

Figure 19: The Load Cell and Experiment Setup for the TMP Compression Tests

Figure 20 shows the optimized TMP being compressed during one of the tests. There are smooth metal plates lubricated with a small amount of oil that come into contact with the top and bottom of the TMP. The lubricated smooth surface allows the shape of the TMP to smoothly deform and prevents additional sliding friction forces from resisting the deformation.

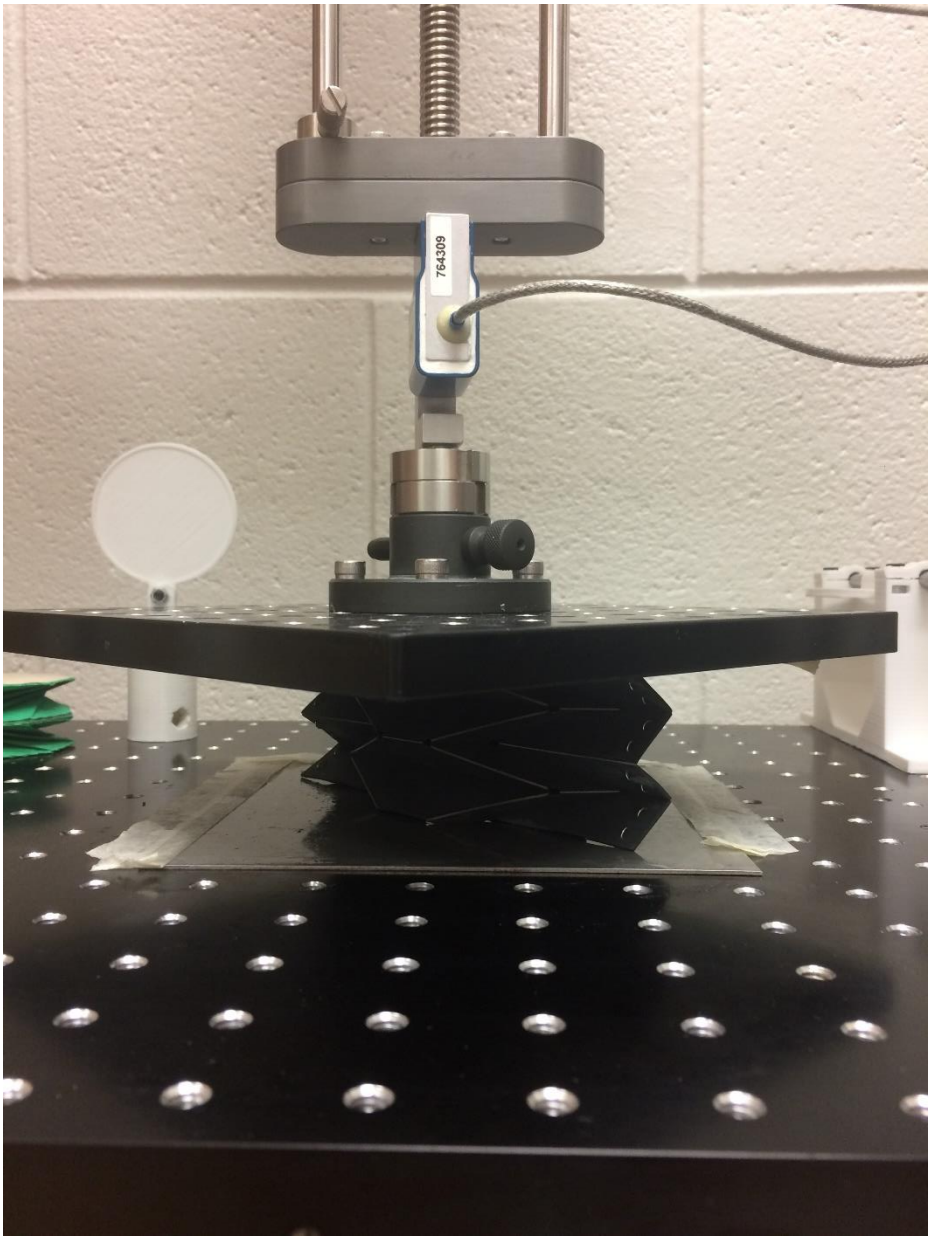

Figure 20: The Optimized TMP Undergoing a Compression Test

Firstly, we want to quantify the effect the groove joint method has on strengthening or weakening the folds. To illustrate this clearly, Figure 21 shows the force displacement curve for the optimized design with all (main and sub) folds weakened (a groove cut into

the mountain) versus an optimized design with the main fold weakened and the sub fold strengthened (groove cut into the valley of the sub folds).

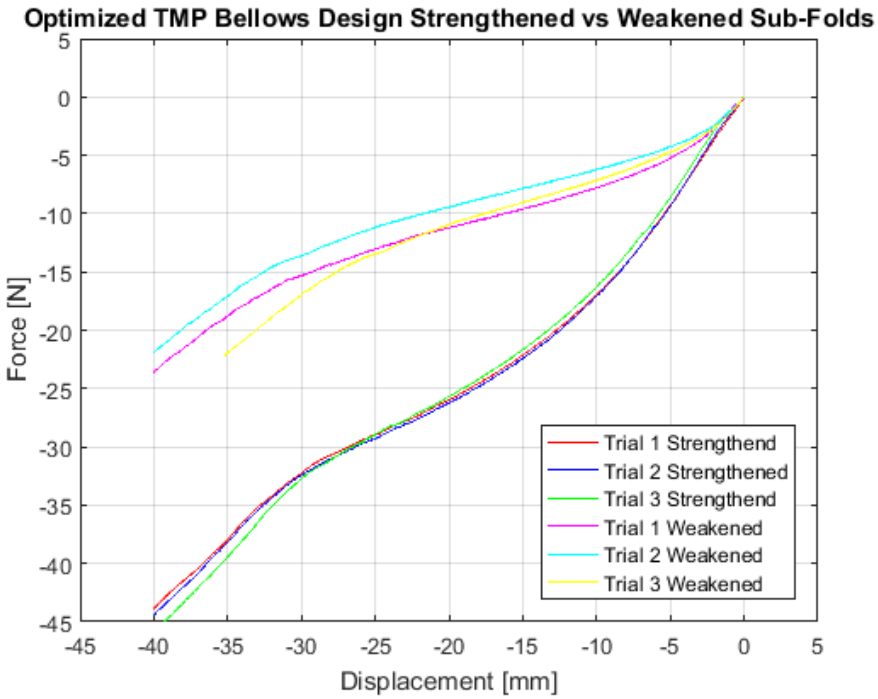

Figure 21: Optimized Design with Strengthened Sub Folds compared to Weakened Sub Folds

We can see an approximate 100% increase in the magnitude of the force generated by the TMP structure with the strengthened sub folds at the displacement limit (40 mm). Strengthening the sub folds and weakening the main folds in this manner allows us to use the simplified force equation for the TMP, equation (29) that accounts for the force generated only by the sub-folds.

To appropriately compare the theoretical force-displacement curve versus the experimental data for the design, the torsional stiffness of the sub folds, k_s, needs to be determined for the structure and used to generate the theoretical curve. To do this I rearrange equation (29) for k_s to obtain:

$$k_s = -\frac{FNdcos(\theta_M)}{32\left[N(\theta_S - \theta_{S_0})\frac{\cos(\frac{\theta_G}{2})^3\sin(\theta_M)}{\cos(\alpha)\sin(\theta_S)}\right]} \tag{32}$$

Using the experimental data obtained by compressing the TMP structure and measuring the force and displacement, I can find a value for k_s at each data point (using the relationships defined in equations (26, 27, and 28) to relate the folding angles to the displacement). The theoretical equation assumes a constant k_s at all displacements so I take the root mean square (RMS) of all experimental values and use that as the k_s in the theoretical model for each design tested. The RMS torsional stiffness is found using equation (33).

$$k_s = \sqrt{\frac{1}{n}\sum_{i=1}^{n} k_{s_i}^2} \tag{33}$$

Where n is the number of data points used across all trials and k_{s_i} is the value found using equation (32) at each data point. The torsional stiffness of the sub folds when strengthened with the groove joint method is found to be $k_s = 0.0409\frac{Nm}{rad}$ with a standard deviation of $1.71\times10^{-4}\frac{Nm}{rad}$ across 3 trials.

3.2 Force Displacement Profile of Original versus Optimized TMP Design

After using the experimental data to backwards calculate the stiffness value as described in the previous section, I can predict the theoretical force displacement curve

with the approximated stiffness value. Figure 22 compares the theoretical force displacement curve for the original design with the optimized design found in section 3.

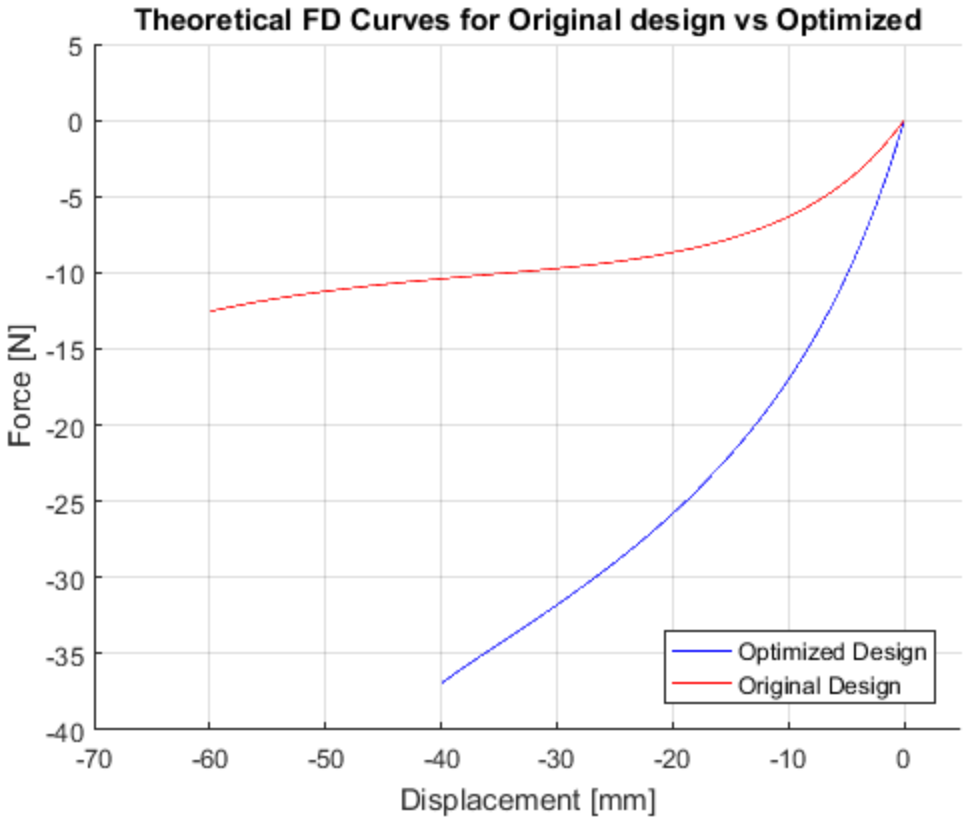

Figure 22: FD Curves for Original Design vs Optimized Design

While the original design has a greater maximum displacement for the same folding ratio of 75%, the optimized design is expected to generate a force that is significantly greater in magnitude, approximately triple the magnitude of the original design at their respective maximum displacements.

Figure 23 compares the experimental results for three trials of both the original design and the optimized design. In both cases, the sub-folds have been strengthened and the main folds weakened using the groove joint explained previously.

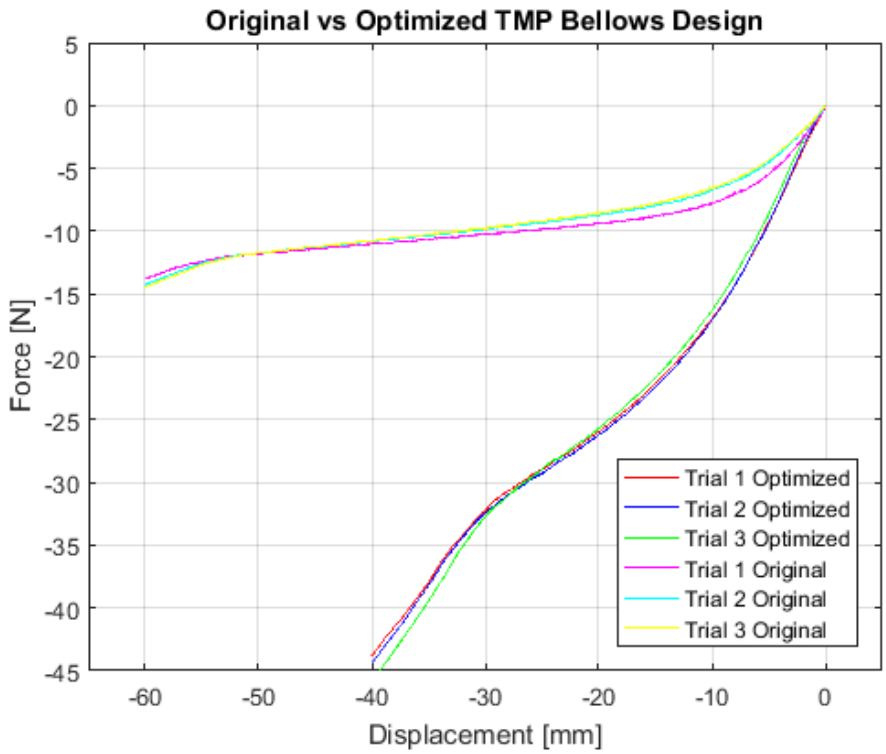

Figure 23: Experimental FD Curves for OG vs Optimized Design

When comparing Figure 22 and Figure 23 we can see that the experimental force displacement curves are in agreement with the predicted theoretical curves. The optimized design while having a smaller structural limit and therefore a smaller maximum displacement, generated considerably more force than the original design. However, it is also necessary to quantify how closely the experimental force-displacement curves are in agreement with the theoretical curves. Figure 24 shows both the theoretical and experimental force displacement curve for the original design.

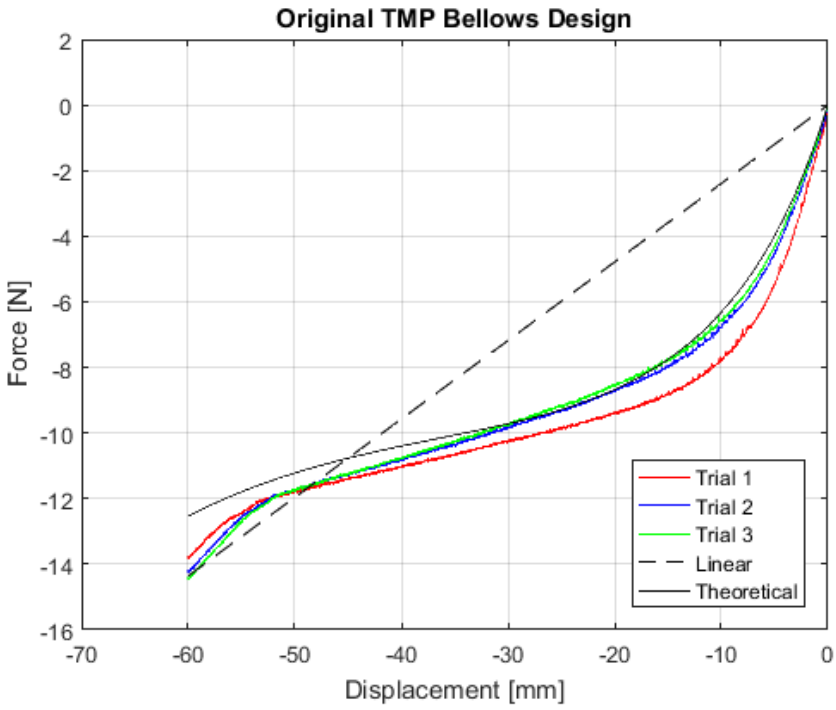

Figure 24: Theoretical vs Experimental FD Curve for Original Design showing Comparable Linear Stiffness

Also included in Figure 24 is a comparable linear force displacement curve that achieves a similar maximum force at the maximum displacement. One can observe the increase in area between the curves and the x-axis for the non-linear TMP bellows curve that signifies the increase in stored elastic energy.

Figure 25 compares the theoretical and experimental force-displacement curve for the optimized design in addition to showing a force displacement curve for comparable linear stiffness.

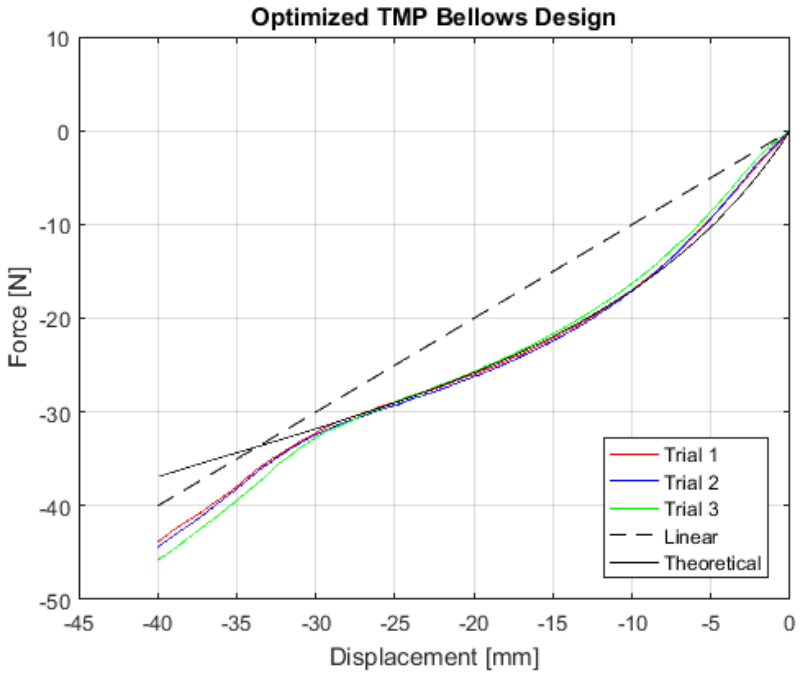

Figure 25: Theoretical vs Experimental FD Curve for Optimized Design showing Comparable Linear Stiffness

Both Figure 24 and Figure 25 show that it is possible to closely predict the force-displacement behavior of the TMP bellows design and we can obtain the expected force-displacement curves in practice. However, as discussed in section 3 it is the stored energy that leads to the increase in jumping performance. To calculate the stored energy, a trapezoidal rule for numerical integration is used on both the experimental and theoretical force displacement curves. Both the experimental and theoretical curves have approximately 8000 data points to generate the curves and calculate the area between them and the x-axis to find the stored energy. Stored energy values for the original and optimized design are shown in Table 4 and Table 5 respectively.

Table 4: Original Design Stored Energy

Original Design Stored Energy [J]					
Trial 1	**Trial 2**	**Trial 3**	**RMS**	**Theoretical**	**% Difference Between Theoretical and Experimental Energy Storage**
0.5811	0.5568	0.5520	0.5634	0.5200	8.02%

Table 5: Optimized Design Stored Energy

Optimized Design Stored Energy [J]					
Trial 1	**Trial 2**	**Trial 3**	**RMS**	**Theoretical**	**% Difference Between Theoretical and Experimental Energy Storage**
0.9784	0.9866	0.9817	0.9822	0.9471	3.64%

With the original design I am able to experimentally obtain within approximately 8% of the predicted stored energy. This value is improved with the optimized design and I am able to obtain within 3.62% of the predicted stored energy. When comparing the stored energy values of the optimized versus the original design, it is observed that the optimized TMP bellows stores approximately 175% of the energy stored by the original design. This further supports the results of section 3 with the optimized design showing improvement on the original concept used for the TMP bellows as the backbone of the jumping mechanism.

3.3 Hysteresis Behavior in the TMP Bellows Force Displacement Profile

As shown in section 3.2, we observe strong agreement in the force-displacement profiles between the predicted theoretical curves and the experimental data when the TMP is compressed form its rest length to the desired folding ratio. However, in the case of

jumping the structure starts from a compressed state and is released back to its rest length. When measuring the force-displacement profile of the TMP from a compressed state back to the rest length, there is significant hysteresis when compared with that of the force-displacement profile measured from rest length to the compressed state. The non-linear profile of the force displacement curve on release loses a significant amount of the energy stored on compression. So much in fact that the jumping behavior is expected to be worse than that of a comparable linear force-displacement profile. In the following section I discuss the problems faced with achieving the desired force-displacement behavior when the TMP bellows is released from a compressed state, as well as an approach taken in an effort to mitigate the hysteresis problem

3.3.1 Percent Energy Loss due to Hysteresis in TMP Bellows

Figure 26 shows the theoretical, the comparable constant linear, and the experimental force-displacement curve for the optimized TMP bellows design. For the experimental curves, the solid lines are measured when compressing the structure form the rest length to the desired initial displacement for jumping, while the dashed lines are measured form the compressed state releasing the structure back to the rest length.

It can be observed that there is significant hysteresis error when measuring the force-displacement response compressing the structure versus measuring while releasing the TMP. When compressing, it can be seen that that the non-linear behavior of the force-displacement curve dips below the comparable constant linear curve and achieves the desired greater stored energy. When releasing however, the non-linear behavior shown is

the exact opposite shape of what is desired. The force-displacement curve rises above the constant linear curve and remains above until returning back to the rest length. Instead of an increase in stored energy over the constant linear curve there is actually a loss of stored energy and the TMP would exhibit worse jumping performance if able to jump at all.

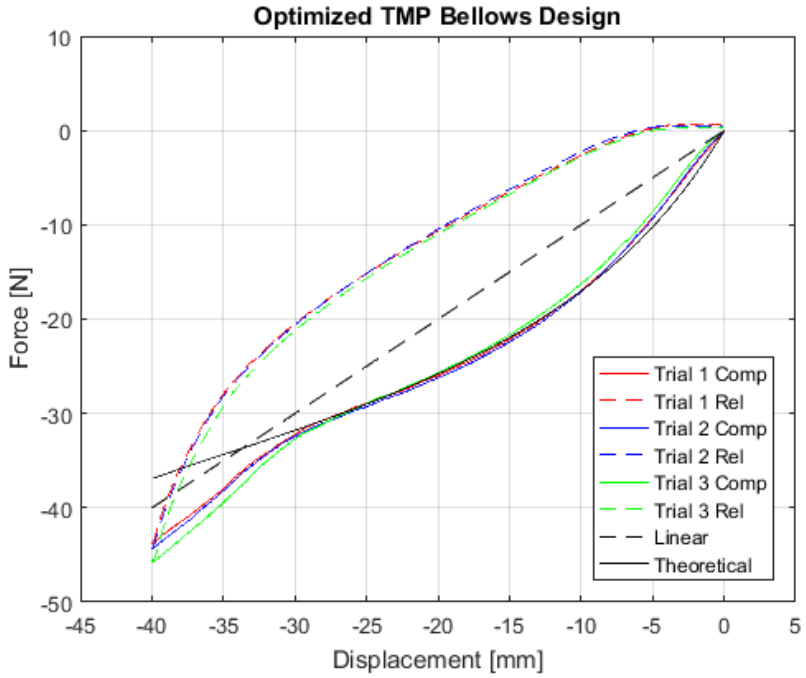

Figure 26: Compression vs Release Force Displacement Curve for Optimized Design

We can quantify the energy lost due to the hysteresis errors as a percentage of the stored energy found when compressing the structure. Table 6 shows the values for the stored energy of each experimental trial as well as the root mean square for the optimized design and the percentage of energy lost, again obtained using trapezoidal numerical integration. It can be seen from the results that roughly half of the energy is lost in the optimized design due to the hysteresis error.

Table 6: Optimized Design Energy Lost due to Hysterical Error

Optimized Design				
	Trial 1	**Trial 2**	**Trial 3**	**RMS**
Compression Energy [J]	0.9784	0.9866	0.9817	0.9822
Release Energy [J]	0.5205	0.5189	0.5405	0.5266
% Loss	46.80%	47.41%	44.94%	46.38%

The same phenomenon with the energy lost from hysteresis error is found when investigating the original design. This suggests that the hysteresis error does not arise strictly as a product of design geometry, rather it may have more to do with the material or the crease line deformation. Figure 27 illustrates the hysteresis error for the original design in a similar manner to Figure 26 for the optimized design.

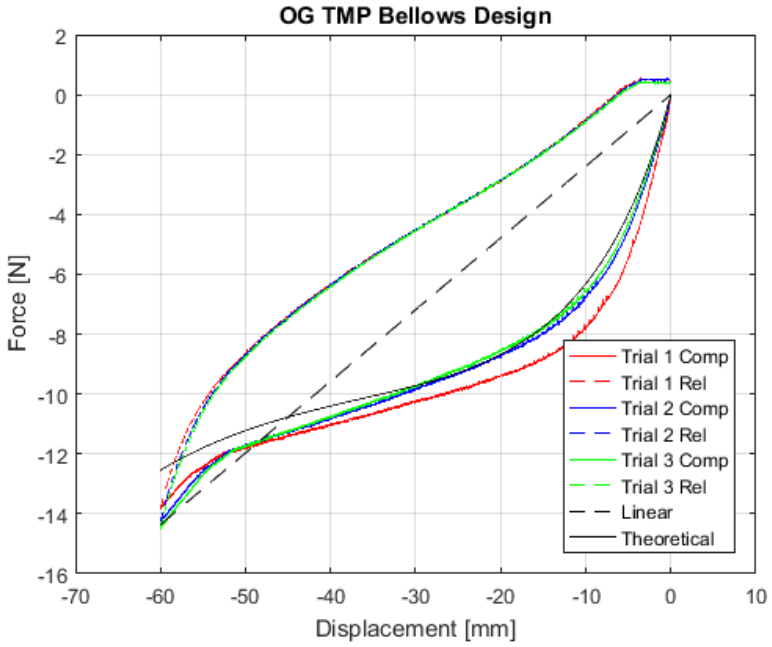

Figure 27: Compression vs Release Force Displacement Curve for Original Design

Table 7 shows the stored energy and percent loss between the compression and release measurements for the original design. Similar values for the percent energy loss are obtained for the original design when comparing with the optimized design.

Table 7: Original Design Energy Lost due to Hysterical Error

Original Design				
	Trial 1	**Trial 2**	**Trial 3**	**RMS**
Compression Energy [J]	0.5811	0.5568	0.5520	0.5633
Release Energy [J]	0.2941	0.2970	0.2992	0.2968
% Loss	49.39%	46.66%	45.80%	47.28%

There could be a number of reasons that contribute to the energy lost when the structure is compressed and then released. The author believes that the most likely culprit is the severe deformation introduced to the material along the crease-lines that leads to material fatigue. Regardless, the TMP bellows will not exhibit the desired jumping performance

unless the hysteresis issue can be solved, and the appropriate shape of the force-displacement curve can be obtained in practice on release as well as compression. The following section discusses one method applied to the TMP in an effort to combat the hysteresis error.

3.3.1 Introducing Torsional Springs to the TMP Bellows Sub-Folds

One method to reduce the plastic deformation while maintaining a large enough torsional stiffness along the sub fold crease lines is to introduce pure linear torsional springs along the sub folds of the TMP structure. The theoretical model of the TMP already treats the torsional stiffness as a linearly constant value and the non-linearity of the force-displacement curve comes from the geometry and folding behavior. Two approaches with torsional springs are used with the optimized design. In the first, I weaken the sub-folds as well as the main folds and rely on the torsional springs to generate the majority of the force necessary for the structure to respond. In the second, the sub folds are strengthened with the groove joint as before, yet I still introduce the torsional springs along the crease lines. The second method relies on the force to be generated by the crease lines and the material themselves while the torsional springs combat the material fatigue and increase the force response upon release.

One of the challenges with introducing the torsional springs is finding components that are small enough to not interfere with the folding behavior of the structure while still generating enough force to overcome the hysteresis energy loss. The torsional springs are mounted by cutting slots in the middle of the sub folds for the center of the springs to align

with the crease lines. The optimized TMP structure with the added torsional springs can be seen in Figure 28.

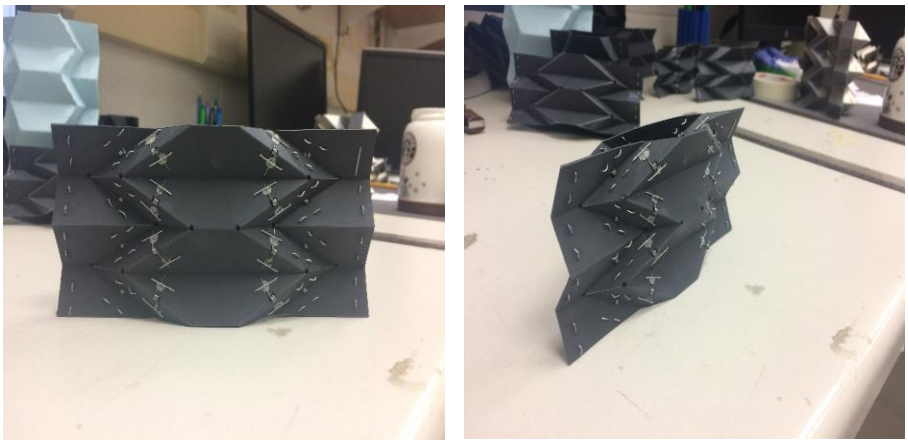

Figure 28: Optimized TMP with Torsional Springs

The force-displacement curve for the optimized design with the torsional springs is measured in the same way as the previous optimized design. The experimental force-displacement curves with weakened sub-folds and added torsional springs are shown in Figure 29. When compared with Figure 21 it can be seen that the magnitude of the force generated by the structure with the torsional springs is similar to that of the TMP with all of the folds weakened. This suggest that the majority of the force response is still coming from the folds themselves and the torsional springs do not have a large enough stiffness value to overcome the hysteresis energy loss. This can also be seen when comparing the release curves to the compression curves in Figure 29.

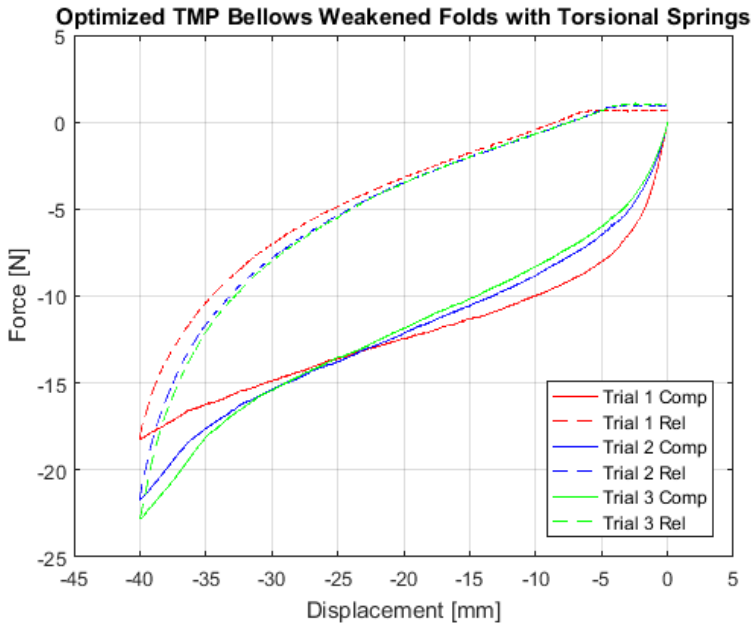

Figure 29: TMP Bellows with Weakened Crease Lines and Torsional Springs mounted along each Sub Fold

Figure 30 shows the force-displacement curves for the TMP with the torsional springs as well as the strengthened sub-folds with the groove joint. Again, it can be seen that the torsional springs do not generate enough force to negate the material fatigue and the hysteresis energy loss. In fact, removing material along the creases to mount the torsional springs decreases the magnitude of the force by a small amount, approximately 5 N at maximum displacement.

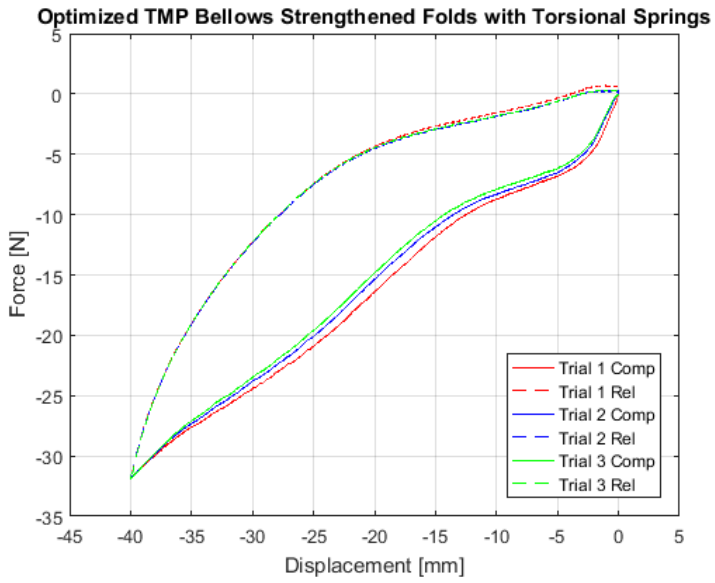

Figure 30: TMP Bellows with Strengthened Crease Lines and Torsional Springs mounted along each Sub Fold

Table 8 and Table 9 show the stored energy for the compressions and release force displacement curves as well as the percent of energy lost on release for the structure with the weakened folds and torsional springs and the TMP with strengthened sub-folds and torsional springs respectively.

Table 8: Stored and Lost Energy for TMP with Torsional Springs and Weakened Sub- Folds

Optimized Design with Weakened Folds and Torsional Springs				
	Trial 1	**Trial 2**	**Trial 3**	**RMS**
Compression Energy [J]	0.4855	0.4823	0.4789	0.4822
Release Energy [J]	0.1823	0.2066	0.2132	0.2007
% Loss	62.45%	57.16%	55.48%	58.37%

Table 9: Stored and Lost Energy for TMP with Torsional Springs and Strengthened Sub-Folds

Optimized with Strengthened Folds and Torsional Springs				
	Trial 1	**Trial 2**	**Trial 3**	**RMS**
Compression Energy [J]	0.6681	0.6447	0.6301	0.6476
Release Energy [J]	0.3113	0.3160	0.3142	0.3138
% Loss	53.41%	50.98%	50.13%	51.51%

As can be seen from the results, approximately half of the stored energy on compression is lost even with the torsional springs. In fact, the structure with the weakened sub folds and mounted torsional springs exhibits the worst energy loss of all TMP designs tested.

Based on the results it appears that the torsional springs used do not generate enough force to negate the hysteresis energy loss of the TMP structure. Increasing the torsional stiffness of the springs may lead to better results, however as mentioned before the springs are limited in their maximum size else they may interfere with the folding behavior of the structure. Increasing the stiffness of the springs tends to come directly from increasing their size and for this study the torsional springs used are close to the limit of what can be implemented with the optimized design without interfering with proper folding behavior.

CHAPTER FOUR

CONCLUSIONS AND RECOMMENDATIONS FOR FUTURE RESEARCH

As a result of this study we have shown that non-linear stiffness can lead to better jumping performance of a jumping mechanism defined by Figure 1 in section 1.2. The non-linear behavior of the force-displacement curve leads to greater stored energy in the non-linear spring elements and this directly translates to improved jumping performance when compared to that of a linear spring, up to a 15% increase in the maximum height achieved by the center of gravity. The maximum height of the center of gravity of the jumping mechanism is directly defined by its maximum potential gravitational potential energy in the post jump phase and the maximum stored potential energy in the compressed state in the pre-jump phase, assuming all stored elastic energy is converted to the kinetic energy of the jump and finally to the maximum potential gravitation energy.

The origami TMP Bellows shows clear non-linear behavior for its force-displacement response of the shape necessary to improve jumping performance as outlined in section 1.3.1. The non-linear behavior arises from the folding behavior and geometry of the structure while still treating the crease lines as having some constant linear torsional stiffness value. This allows us to use evolutionary algorithm optimization techniques on 2500 designs outlined by constraints set for ease of manufacturing to find the best possible design for optimum theoretical jumping performance. Starting with an initial design outlined in section 2.1 and the design constraints outlined in Table 1and Table 2, I am able to obtain the optimum design defined by the geometric parameters in Table 3. This optimum design achieves the best jumping performance based on the numerical

simulations that solve the dynamics of the jumping mechanism outlined in section 1.2 and the objectives for airtime and clearance of the bottom mass.

When designing the TMP bellows and manufacturing the structure based on the initial and optimized design out of polypropylene plastic sheets I am able to show greater than 90% agreement between the expected force-displacement curve that arises from equation (29) and the curves obtained from experimental data. Additionally, I am able to show the benefits of the optimized design over the original in terms of its maximum stored energy when subject to a desired displacement based on a folding ratio of 75%. This further supports the claim of improved jumping performance for a jumping mechanism that utilizes non-linear stiffness elements as a means of increasing the stored elastic energy.

The problem of nearly 50% hysteresis energy loss when releasing the TMP structure from its compressed state however inhibits experimental confirmation of the jumping behavior and performance obtained from the optimization results shown in Table 3. Using linear torsional springs to negate the effect of plastic deformation in the material along the crease lines did not adequately solved the problem of the hysteresis energy loss. The torsional springs were not strong enough to overcome the energy loss due to material fatigue in the crease lines. Torsional springs with a stiffness of greater magnitude may improvements in terms of less energy loss, however due to size constraints with the optimum TMP design to ensure proper folding behavior, I am limited in increasing the size of the springs and therefore increasing their stiffness values.

Further research should focus on combating the hysteresis energy loss of the TMP structure when releasing from the compressed state. The TMP bellows is proven to exhibit

the desired non-linear behavior that can lead to improved jumping performance when compressed from the rest length. Strong correlation between the theoretical force-displacement curve and experimental test results, as well as an already established optimization procedure for the design will allow for easy adjustments to be made to the design if necessary to negate the hysteresis energy loss. Investigating the specifics of where the energy loss arises and how it relates to the TMP design, The energy loss can be negated and the TMP dynamic jumping behavior can be experimentally tested and compared with the numerical simulations to confirm the model and the benefits of non-linear spring elements in jumping mechanisms. Additionally, if the hysteresis energy loss can be explained and modeled, this opens the door for other studies on the dynamics of origami structures. Damping is a known problem within origami structures that arises from plastic deformation along the creases. If the damping can be modeled and related to the hysteresis, we can begin to account for it in our theoretical and experimental models thus allowing us to more accurately predict the behavior of origami structures in different applications.

APPENDICES

Appendix A

Graphtec FCX4000 Specifications

Item	FCX4000-50ES	FCX4000-60ES (stand optional)
Configuration	Digital servo system, Flatbed	
Media hold-down method	Electrostatic panel	
Effective cutting area	W 25.98" x H 19.21"	W 38.4" x H 25.9"
Mountable media (Y-axis direction)	21.10"	27.97"
Maximum cutting speed	29.5"/s (1 to 75 cm/s in 23 steps)	
Cutting pressure	Tool 1: Max. 5.88 N (600 gf) Tool 2: Max. 5.88 N (600 gf)	
Cutting force settings	Tool 1: in 48 steps, Tool 2: in 48 steps	
Minimum character size	Approx. 10 mm square (varies with character font and media)	
Mechanical resolution	0.005 mm (5µm)	
Programmable resolution	GP-GL mode: 0.1/0.05/0.025/0.01 mm, HP-GL™ (*1) : 0.025 mm	
Distance accuracy	Max.0.2% of the distance moved or 0.1mm, whichever is larger (excluding contraction of media, in plotting/cutting mode) (*2)	
Perpendicularity	Max 0.3 mm / 16.93" (excluding contraction	Max 0.4 mm / 24.01" (excluding contraction

Item	FCX4000-50ES	FCX4000-60ES (stand optional)
	of media, in plotting/cutting mode)	of media, in plotting/cutting mode)
Repeatability	Max 0.1mm (excluding contraction of media, in plotting/cutting mode) (*2)	
Standard interfaces	USB2.0 (Full Speed) / RS-232C / Ethernet (10BASE-T/100BASE-TX)	
Buffer memory	2MB	
Command sets	GP-GL / HP-GL™ / AUTO (Automatic switching in GP-GL and HP-GL™)	
Number of tools	2 tools	
Cutter blade, pen, and tool types	Cutter blade: supersteel Pen: water-based fiber-tip pen Creasing/scoring tool	
Operating panel	3.7-inch graphical LCD (same LCD as the FCX2000)	
New features	Dual configuration, Creasing in the curve, Perforation cutting (performed by the force control), Data management using the bar-code, Offline cutting operation using the USB memory, Display the degree of wear for the cutting blade, Confirming the cutting object size, Draft mode (higher throughput in arc)	
Power supply	100 to 240 V AC, 50/60 Hz (Auto switching)	
Power consumption	Max. 120 VA	
Operating environment	Temperature: 10 to 35 degree C , Humidity: 35 to 75% RH (non-condensing)	

Item		FCX4000-50ES	FCX4000-60ES (stand optional)
Guaranteed accuracy environment		Temperature: 16 to 32 degree C, Humidity: 35% to 70% RH (non-condensing)	
External dimensions (*3) (W x D x H)		W 42.87" x D 35.31" x H 8.03"	W 55.31" x D 42.08" x H 8.03" (including stand : W 55.31" x D 43.18" x H 35.27")
Weight		approx. 63.93 lbs (29kg)	approx. 83.77 lbs (38 kg) (including stand 121.25 lbs (55 kg)
Compatible OS (*4)(*5)		Windows 10 (Home / Pro / Enterprise / Education) Windows 8.1 (Windows 8.1 / Pro / Enterprise) Windows 8 (Windows 8 / Pro / Enterprise) Windows 7 (Ultimate / Enterprise / Professional / Home Premium)	
		Mac OS X 10.7 to 10.11 / macOS 10.12 (Sierra) to 10.13 (High Sierra)	
Supported software		Cutting Master 4, Graphtec Pro Studio, Graphtec Studio for Mac, Windows Driver	
Compatible Standards	Safety	UL/cUL, CE mark	
	EMC	VCCI Class A, FCC Class A, CE mark (EN55032, others)	

Table A-1: FCX 4000 Specifications.

Appendix B

ADMET Expert 5601 Tensile Testing Machine Specifications

Actuator Model		5601 Static	5602 Static	5603 Static	5951 Dynamic	5952 Dynamic	5955 Dynamic
Continuous Force	lbf kN kgf	225 1 100	500 2.2 225	1,000 4.5 450	500 2.5 250	1,125 5 500	2,250 10 1,000
Peak Force	lbf kN kgf	- - - - - -	- - - - - -	- - - - - -	900 4 400	1,800 8 800	3,150 14 1,400
Maximum Speed	in/min mm/min	25 635	7 178	20 504	800 20,320	600 15,240	600 15,240
Actuator Stroke	in mm	12 305	12 305	12 305	6 152	6 152	6 152
Position Resolution	µin µm	2.9 0.073	0.87 0.022	2.2 0.057	100 2.54	50 1.27	50 1.27
Throat Depth when mounted on 1 Column Frame	in mm	3.5 89	3.5 89	3.5 89	- - - -	- - - -	- - - -
Maximum Power	VA	100	100	250	1,760	2,800	3,600
Single Phase Voltage	VAC Hz	100-240 47-63	100-240 47-63	110,220 50,60	220 50,60	220 50,60	220 50,60

Figure B-1: Expert 5601 Static Specifications

REFERENCES

[1] P. Y. Chua, T. Ilschner, and D. G. Caldwell, “Robotic manipulation of food products - A review,” *Ind. Rob.*, vol. 30, no. 4, pp. 345–354, 2003.

[2] A. Shukla and H. Karki, “Application of robotics in onshore oil and gas industry-A review Part i,” *Rob. Auton. Syst.*, vol. 75, pp. 490–507, 2016.

[3] R. Bogue, “Robots in the nuclear industry: A review of technologies and applications,” *Ind. Rob.*, vol. 38, no. 2, pp. 113–118, 2011.

[4] A. H. Reddy, B. Kalyan, and C. S. N. Murthy, “Mine Rescue Robot System – A Review,” *Procedia Earth Planet. Sci.*, vol. 11, pp. 457–462, 2015.

[5] F. B. V. Benitti, “Exploring the educational potential of robotics in schools: A systematic review,” *Comput. Educ.*, vol. 58, no. 3, pp. 978–988, 2012.

[6] T. Belpaeme, J. Kennedy, A. Ramachandran, B. Scassellati, and F. Tanaka, “Social robots for education: A review,” *Sci. Robot.*, vol. 3, no. 21, p. eaat5954, 2018.

[7] P. K. Jamwal, S. Hussain, and S. Q. Xie, “Review on design and control aspects of ankle rehabilitation robots,” *Disabil. Rehabil. Assist. Technol.*, vol. 10, no. 2, pp. 93–101, 2015.

[8] H. Robinson, B. MacDonald, and E. Broadbent, “The Role of Healthcare Robots for Older People at Home: A Review,” *Int. J. Soc. Robot.*, vol. 6, no. 4, pp. 575–591, 2014.

[9] J. Liu, M. Tan, and X. Zhao, “Legged robots — an overview,” *Trans. Inst. Meas. Control*, vol. 29, no. 2, pp. 185–202, 2007.

[10] Z. Hongchao, G. A. O. Haibo, D. Zongquan, D. Liang, and L. I. U. Zhen, “A review

of heavy-duty legged robots," vol. 57, no. 2, pp. 298–314, 2014.

[11] S. Dubey and E. Studies, "Robot Locomotion – A Review," no. December, 2015.

[12] A. Sayyad, B. Seth, and P. Seshu, "Single-legged hopping robotics research — A review," vol. 25, no. 2007, pp. 587–613, 2019.

[13] J. Zhao *et al.*, "MSU jumper: A single-motor-actuated miniature steerable jumping robot," *IEEE Trans. Robot.*, vol. 29, no. 3, pp. 602–614, 2013.

[14] D. W. Haldane, M. M. Plecnik, J. K. Yim, and R. S. Fearing, "Robotic vertical jumping agility via series-elastic power modulation," *Sci. Robot.*, vol. 1, no. 1, p. eaag2048, 2016.

[15] A. Schammass, G. A. P. Caurin, and C. M. O. Valente, "Control of a One-Legged Robot with Energy Savings," *Brazilian Soc. Mech. Sci*, vol. 23, no. 1, pp. 41–48, 2001.

[16] J. Albro and J. Bobrow, "Optimal Motion Primitives for a 5 DOF Experimental Hopper," pp. 3630–3635, 2001.

[17] S. Sadeghi, B. D. Betsill, P. Tallapragada, and S. Li, "THE EFFECT OF NONLINEAR SPRINGS IN JUMPING MECHANISMS," pp. 18–21, 2018.

[18] S. E. Bergbreiter, "Autonomous jumping microrobots," *ProQuest Diss. Theses*, vol. 3306062, p. 150, 2007.

[19] J. Zhang, G. Song, G. Qiao, T. Meng, and H. Sun, "An Indoor Security System with a Jumping Robot as the Surveillance Terminal," *IEEE Trans. Consum. Electron.*, vol. 57, no. 4, pp. 1774–1781, 2011.

[20] U. Scarfogliero, C. Stefanini, and P. Dario, "The use of compliant joints and elastic

energy storage in bio-inspired legged robots," *Mech. Mach. Theory*, vol. 44, no. 3, pp. 580–590, 2009.

[21] J. Zhao, N. Xi, B. Gao, M. W. Mutka, and L. Xiao, "Design and Testing of a Controllable Miniature Jumping Robot," *2010 IEEE/RSJ Int. Conf. Intell. Robot. Syst.*, pp. 3346–3351, 2010.

[22] H. Tsukagoshi, M. Sasaki, A. Kitagawa, and T. Tanaka, "Design of a Higher Jumping Rescue Robot with the Optimized Pneumatic Drive," no. April, pp. 76–83, 2005.

[23] S. Kesner, J. Plante, S. Dubowsky, and P. Boston, "a Hopping Mobility Concept for a Rough Terrain Search and Rescue Robot," *Adv. Climbing Walk. Robot. Proc.*, pp. 271–280, 2007.

[24] S. Dubowsky, S. Kesner, J. S. Plante, P. Boston, S. Dubowsky, and P. Boston, "Hopping mobility concept for search and rescue robots," 2015.

[25] A. Yamada, M. Watari, H. Mochiyama, and H. Fujimoto, "An Asymmetric Robotic Catapult based on the Closed Elastica for Jumping Robot," pp. 232–237, 2008.

[26] A. Yamada, H. Mameda, H. Mochiyama, and H. Fujimoto, "A compact jumping robot utilizing snap-through buckling with bend and twist," *IEEE/RSJ 2010 Int. Conf. Intell. Robot. Syst. IROS 2010 - Conf. Proc.*, pp. 389–394, 2010.

[27] P. Fiorini and J. Burdick, "The development of hopping capabilities for small robots," *Auton. Robots*, vol. 14, no. 2–3, pp. 239–254, 2003.

[28] E. T. Filipov, T. Tachi, and G. H. Paulino, "Origami tubes assembled into stiff , yet reconfigurable structures and metamaterials," vol. 112, no. 40, pp. 12321–12326,

2015.

[29] S. Felton, M. Tolley, E. Demaine, D. Rus, and R. Wood, “A method for building self-folding machines,” vol. 345, no. 6197, pp. 8–11, 2014.

[30] M. Johnson *et al.*, “Fabricating biomedical origami : a state-of-the-art review,” pp. 2023–2032, 2017.

[31] P. Wang, T. A. Meyer, V. Pan, P. K. Dutta, and Y. Ke, “The Beauty and Utility of DNA Origami,” *Chem*, vol. 2, no. 3, pp. 359–382, 2017.

[32] H. Fang, S. Li, and K. W. Wang, “Self-locking degree-4 vertex origami structures,” 2016.

[33] S. Li, H. Fang, S. Sadeghi, P. Bhovad, and K. W. Wang, “Architected Origami Materials: How Folding Creates Sophisticated Mechanical Properties,” *Adv. Mater.*, vol. 31, no. 5, pp. 1–18, 2019.

[34] H. Fang, S. Li, H. Ji, and K. W. Wang, “Dynamics of a bistable Miura-origami structure,” *Phys. Rev. E*, vol. 95, no. 5, p. 052211, 2017.

[35] S. Sadeghi and S. Li, “Harnessing the Quasi-Zero Stiffness From Fluidic Origami for Low Frequency Vibration Isolation,” *Vol. 2 Model. Simul. Control Adapt. Syst. Integr. Syst. Des. Implementation; Struct. Heal. Monit.*, p. V002T03A008, 2017.

[36] H. Yasuda and J. Yang, “Reentrant origami-based metamaterials with negative Poisson’s ratio and bistability,” *Phys. Rev. Lett.*, vol. 114, no. 18, pp. 1–5, 2015.

[37] H. Yasuda, T. Yein, T. Tachi, K. Miura, and M. Taya, “Folding behaviour of Tachi – Miura polyhedron bellows,” *Proc. R. Soc. A Math. Phys. Eng. Sci.*, vol. 469:201303, no. August, pp. 1–18, 2013.

[38] C. Lee, V. N. Goverdovskiy, and A. I. Temnikov, “ARTICLE IN PRESS Design of springs with ‘“ negative ”’ stiffness to improve vehicle driver vibration isolation,” vol. 302, pp. 865–874, 2007.

[39] Y. Wang, S. Li, S. A. Neild, and J. Z. Jiang, “Comparison of the dynamic performance of nonlinear one and two degree-of-freedom vibration isolators with quasi-zero stiffness,” *Nonlinear Dyn.*, vol. 88, no. 1, pp. 635–654, 2017.

[40] S. Sadeghi, B. Betsill, and S. Li, “Design and Optimization of an Origami-Inspired Jumping Mechanism with Nonlinear Stiffness Properties,” pp. 1–8, 2019.

[41] K. Liu and G. H. Paulino, “Nonlinear mechanics of non-rigid origami : an efficient computational approach † Subject Areas :,” 2017.

[42] K. Deb, A. Member, A. Pratap, S. Agarwal, and T. Meyarivan, “A Fast and Elitist Multiobjective Genetic Algorithm :,” vol. 6, no. 2, pp. 182–197, 2002.

[43] I. L. Delimont, S. P. Magleby, and L. L. Howell, “Evaluating Compliant Hinge Geometries for Origami-Inspired Mechanisms,” *J. Mech. Robot.*, vol. 7, no. 1, p. 011009, 2015.